Applied Thermal Engineering 291 (2026) 130203

Contents lists available at ScienceDirect

Applied Thermal Engineering

journal homepage: www.elsevier.com/locate/apthermeng

Research Paper

Impact of flame kernel formation process on ultra-lean hydrogen combustion in spark-ignition engines: modeling and experimental validation

F. Bozza [a], V. De Bellis [a], L. Teodosio [a,*], M. Pretto [b], P. Giannattasio [b], R. Novella [c], J. Gomez-Soriano [c]

[a] Industrial Engineering Department, Mechanic and Energetic Section, University of Naples "Federico II", via Claudio 21, 80125 Naples, Italy
[b] University of Udine, Polytechnic Department of Engineering and Architecture, via delle Scienze 206, 33100 Udine, Italy
[c] CMT - Clean Mobility & Thermofluids, Universitat Politècnica de València, Camino de vera s/n, 46022, Valencia, Spain

ARTICLE INFO

Keywords:
Hydrogen flame
Flame kernel expansion
Ultra-lean SI engine
0D/1D modeling
Flame instability

ABSTRACT

Ultra-lean operation of hydrogen-fueled spark-ignition (SI) engines is a promising solution for the ongoing energy transition, but simulation of their performance poses a major challenge due to the complex interaction between thermo-diffusive (TD) flame instability and in-cylinder turbulence. This interaction influences even the flame kernel (FK) formation process, whose significant impact on the engine performance has so far been estimated primarily through experimental evidence. Here, this estimation is conducted by integrating a FK model recently proposed by the authors into a 0D/1D engine simulation framework formulated within a commercial software package. The FK model provides a 1D description of an expanding spherical kernel based on the transient thermo-diffusive theory through laminar flame speed, activation energy, and Lewis number. From the FK model outputs, a kernel duration is defined and used as a delay between spark timing and start of combustion in the 0D/1D simulation. Consolidated literature sub-models account for TD instability and turbulence effects during both FK formation and in-cylinder combustion, simulating the latter with a phenomenological approach. The model predictions are compared with experimental outcomes from a single-cylinder hydrogen-fueled SI engine operated at 1500 rpm, different loads (3–8 bar BMEP) and multiple equivalence ratios (0.25–0.71). The instability-affected FK delays are captured well in all 21 operating points tested, leading to substantial improvements in the prediction of pressure cycles, burn rates, combustion angles, BMEPs, and NOx emissions. The accuracy of the proposed 0D/1D simulation makes it suitable for 'virtual engine' applications aimed at fast calibration and testing of alternative designs.

1. Introduction

Nowadays, worldwide efforts are focused on reducing greenhouse gas and noxious emissions to curb air pollution and global warming [1], to which the transport sector is a key contributor due to the widespread use of internal combustion engines (ICEs) fed with hydrocarbon fuels, whose combustion releases harmful compounds [2]. The stringent emission targets imposed by current international regulations are forcing a strong push toward alternative solutions, such as the transition to cleaner low- or zero-carbon fuels or the employment of hybrid electric powertrains, battery electric vehicles, and fuel cells (FCs) [3–5]. Among these options, hydrogen ICEs appear very suitable for long-distance transport as well as off-road and light-duty vehicles, especially in a spark-ignition (SI) configuration [6,7], showing also significant benefits over FCs thanks to better adherence to circular economy principles, higher tolerance to fuel contamination, and easy retrofitting of existing ICEs [8].

Despite these promises, the widespread adoption of hydrogen ICEs is hindered by several factors. A relevant one is the low volumetric energy density of hydrogen, which makes its efficient storage very complex and ultimately results in a lower power output compared to gasoline SI units [9–12]. Moreover, hydrogen ICEs are susceptible to abnormal combustion phenomena (e.g. pre-ignition, backfiring), which require specific countermeasures such as direct injection and/or ultra-diluted mixtures. However, while ultra-diluted combustion is actually advantageous

* Corresponding author.
E-mail address: luigi.teodosio@unina.it (L. Teodosio).

https://doi.org/10.1016/j.applthermaleng.2026.130203
Received 28 November 2025; Received in revised form 3 February 2026; Accepted 7 February 2026
Available online 10 February 2026

Nomenclature

Symbols

$A_{(L/T)}$	Area (of laminar / turbulent flame front)
$B_{1,2,3}$	Flame instability parameter coefficients
c_{Ka}	Flame instability tuning constant
c_p	Specific heat at constant pressure
c_Σ	Flame wrinkling factor correction
$C_{A,T}$	Adjustment coefficients for flame kernel model
C_d	Entrainment area
d	Distance
D	Mass diffusivity
D_3	Fractal dimension
E	Energy
$f_{uT/Y}$	Normalized thicknesses for flame kernel model
h	Absolute enthalpy
k	Thermal conductivity, turbulent kinetic energy
Ka	Karlovitz number
l_T	Thermal flame thickness
L_i	Integral length scale
$L_{min/max}$	Minimum / maximum flame wrinkling length scale
$Le_{(D/E/eff)}$	(Deficient / excess / effective) Lewis number
m	Mass
$\dot{m}_{en}$	Entrainment mass flow rate
p	Pressure
P	Power
Pr	Prandtl number
r	Radius or radial coordinate
R	Normalized radius
R_0	Ideal gas constant
S	Flame speed relative to the unburned mixture
S_F	Unstable laminar flame speed
S_S	Unstable turbulence-affected (effective) flame speed
t	Time
T	Temperature
U	Normalized expansion velocity
u'	Turbulence intensity
v	Absolute expansion velocity
V	Volume
x_r	Inert gas fraction
y	Normalized mass fraction
Y	Mass fraction
Ze	Zeldovich number

Greek symbols

β	Weighting parameter for effective Lewis number
γ	Heat capacity ratio
δ	Thickness
ε	Turbulent kinetic energy dissipation rate
η	Energy deposition efficiency, Kolmogorov length scale
θ, Θ	Normalized temperature
ϑ	Jacobi theta function
μ	Dynamic viscosity
$\Pi_{(crit)}$	Normalized (critical) pressure
ρ	Density
Σ	Flame wrinkling factor
τ	Normalized time
ϕ	Normalized radial coordinate, equivalence ratio
φ	Corrected equivalence ratio
ω_f	Normalized reaction rate
ω_2	Flame instability parameter

Subscripts and superscripts

$[\cdot]_a$	Activation
$[\cdot]_A$	Deficient reactant
$[\cdot]_{ad}$	Adiabatic flame
$[\cdot]_b$	Burned
$[\cdot]_{bd}$	Electrical breakdown
$[\cdot]_e$	Electric(al)
$[\cdot]_{end}$	End condition
$[\cdot]_f$	Flame or flame kernel
$[\cdot]_g$	Spark gap
$[\cdot]_i$	Initial
$[\cdot]_L$	Laminar
$[\cdot]_u$	Unburned
$[\cdot]_{turb+TD}$	Affected by turbulence and TD instability
$[\cdot]^0$	Reference

Acronyms

0D/1D/3D	Zero/one/three-dimensional
ABDC	Reference
A(C/F)TDC	After (combustion/firing) top dead center
BBDC	Before bottom dead center
BMEP	Brake mean effective pressure
BTDC	Before top dead center
CAD	Crank angle degree
CFD	Computational fluid dynamics
CoV	Coefficient of variation
DL	Darrieus-Landau
FC	Fuel cell
FK	Flame kernel
HRR	Heat release rate
ICE	Internal combustion engine
IMEP	Indicated mean effective pressure
LFS	Laminar flame speed
MFB_x	x% of mass fraction burned
NO_x	Nitrogen oxides
OP	Operating point
SI	Spark ignition
SoC	Start of combustion
ST	Spark timing
TD	Thermo-diffusive
TPA	Three-pressure analysis

thanks to its lower flame temperatures, which reduce both wall heat losses and NO_x emissions [13], it is also challenging to control [12]. A key reason behind it is the instability of lean hydrogen/air flames, whose impact on the combustion speed is complex and not yet fully clarified [14].

Dedicated investigations into flame instability show that lean hydrogen/air flames can undergo two types of instabilities. The first type is the Darrieus-Landau (DL) instability, which is caused by the sudden gas density change across the flame. This induces strong hydrodynamic disturbances on the flame surface, whose ultimate effect is increasing the combustion speed [15]. The second type is the thermo-diffusive (TD) instability, which emerges specifically in lean hydrogen/air mixtures due to the higher mass diffusivity of the limiting reactant, H_2, compared to the thermal diffusivity of the mixture (i.e. Lewis number $Le < 1$). This generates preferential diffusion effects as H_2 approaches the reaction zone, resulting in greater local reaction rates that increase the fuel burn rate and hence the flame speed [16]. Both instabilities generate cellular structures causing the self-wrinkling of the flame, but the DL cells are larger than the TD ones [17]. Moreover, while the DL effects can be neglected at high pressures, the TD effects become

increasingly relevant as the pressure rises, influencing even the early flame kernel (FK) growth in spark-driven processes [18]. Therefore, for reliable modeling of hydrogen-fueled SI engines, focusing on the FK formation while accounting for the simultaneous presence of TD instability and in-cylinder turbulence becomes crucial.

Concerning the FK development in SI engines, the research has been conducted following a variety of approaches. For instance, an empirical correlation was developed by Giménez et al. [19] to predict the FK duration from 48 operating points of a SI engine fueled with natural gas, hydrogen, and their mixtures, which yielded good results for their case but lacked general validity. Instead, Keum et al. [20] proposed a semi-empirical FK model to reproduce the laminar-to-turbulent flame transition, but validation against the experimental outcomes of a propane-fueled combustion bomb was achieved only after recalibrating the FK model parameters. This lack of generality is typical of empirical formulations, and attempts to overcome it have been carried out using analytical FK expansion models. However, most of them derive from the historical work by Herweg and Maly [21], who proposed a FK model based on mass and energy conservation laws capable of accounting for multiple engine parameters (ignition system, unburned mixture, flow field). A notable limit of this model is the too simplified description of flame stretch through a linear correlation, but this simplicity also favored its application in CFD-based simulations. As an example, Fan et al. [22] used Lagrangian marker particles to track the FK location developing in a hydrocarbon-fueled SI engine. Recently, FK models of this kind have been applied also to the simulation of combustion in lean hydrogen SI engines, conducted either adopting a fully 3D CFD approach [23] or using Herweg and Maly's model up to a fixed value of the kernel radius followed by a G-equation approach [24]. The latter work is rather interesting, as good agreements with the experiments on the FK formation were observed in conjunction with a noticeable underestimation of the pressure cycle for some operating conditions. This difficulty in modeling the impact of the instability-affected FK formation on the performance of (ultra-)lean hydrogen SI engines is yet to be solved, as shown by the need for extensive experimental evidence demonstrated in very recent contributions [25] [26].

In this work, the open problem of estimating the impact of the FK formation on (ultra-)lean hydrogen combustion in SI engines is tackled by using a 1D FK model of general validity recently proposed by the present authors [27]. This model is based on the transient thermo-diffusive theory of flames [28], which considers the temperature and reactant gradients upstream of the flame sheet to estimate the kernel expansion speed, and accounts also for the high-temperature ionization and dissociation effects associated with the SI process. This FK model, recently tested on laminar hydrogen flames [29], is here extended to hydrogen-fueled SI engines by coupling it with Howarth et al.'s formulation of TD instability [30] to estimate the FK formation time or duration. This is then incorporated into a 0D/1D model of the SI engine, developed in a GT-Power™ environment, to simulate the entire TD-unstable in-cylinder turbulent combustion. The 0D/1D model is validated against the outcomes of a dedicated experimental investigation performed on a single-cylinder hydrogen SI engine operated at different equivalence ratios and load levels. Its predictive capabilities are proved with reference to FK duration, in-cylinder combustion, engine performance, and NO_x emissions. The main novelties and merits of this work can be summarized as follows:

- provision and validation of a modeling method for accurate prediction of the FK growth after a spark ignition, with special emphasis on the unstable combustion of lean hydrogen;
- demonstration of the strong impact of a well-predicted FK formation on the overall performance and emissions of a hydrogen-fueled SI engine;
- use of a 0D/1D simulation framework, whose low computational burden compared to 3D CFD methods enables easy set-up of a 'virtual engine' for multiple practical applications, such as fast engine calibration, simulation of new designs, and/or modifications to current units [31].

The article is structured as follows. First, the authors' FK model is briefly recalled in Section 2, and the methodology to estimate all relevant flame properties is presented and validated for three different fuels in Section 3. Then, in Section 4 a criterion is established to identify the FK duration when using a typical automotive ICE spark plug, and the impact of the key flame parameters on this duration is examined. In Section 5, the predicted FK durations are compared with the outputs of a dedicated experimental investigation involving 21 operating points (OPs) of an ultra-lean hydrogen SI engine, highlighting the key role of the TD instability. Finally, in Section 6 the FK model is integrated into the 0D/1D model of the aforementioned engine alongside phenomenological sub-models that cover in-cylinder turbulence, large-scale TD instability, and NO_x formation. The 0D/1D engine model is applied to predict combustion onset, burn rates, and trends of global performance and NO_x emissions for all the 21 engine OPs. The conclusions are drawn in Section 7.

2. The flame kernel model

The model adopted to describe the initiation and expansion of a spark-ignited flame kernel was presented recently by the authors [27,32], and in this section it is only briefly recalled.

On a fundamental level, the FK model is split into ignition and early expansion stages. The ignition coincides with the electrical breakdown between the plug electrodes, which results in the formation of a plasma column that expands via a mostly cylindrical shock wave to release the local overpressure, gradually increasing its mass. The initial conditions for the kernel expansion stage, inspired by the work of Meyer and Wimmer [33] and here denoted by subscript i, are established upon the extinction of the shock wave at the end of the breakdown. These conditions, calculated using Eqs. (1), consist of plasma column radius $r_{i,cyl}$, its absolute enthalpy h_i, and the time t_i required for pressure equalization following the shock wave:

$$\begin{cases} r_{i,cyl} = 0.5 r_c = 0.5 \left(\dfrac{E_{bd}}{3.94 \pi d_g p_u} \right)^{1/2} \\ t_i = 1.5 t_c = 1.5 \left(\dfrac{r_c}{\sqrt{\gamma_u p_u / \rho_u}} \right) \\ (h_i - h_u) \rho_i V_i = \eta_{bd} E_{bd}, \quad \text{with } V_i = \pi r_{i,cyl}^2 d_g \end{cases} \tag{1}$$

In Eqs. (1), whose functional dependencies appear to hold true also following experimental tests at multiple pressure levels [34], r_c and t_c are the characteristic length and time scales, while E_{bd} denotes the breakdown energy deposited across spark gap d_g with efficiency η_{bd}. For the mixture-related quantities, p_u is the ambient pressure, assumed uniform, γ_u, ρ_u, and h_u are the heat capacity ratio, the density and the enthalpy of the unburned mixture, respectively, and V_i is the plasma volume. Initial temperature T_i is derived from absolute enthalpy h_i under the assumption of chemical equilibrium at known p_u. Finally, since the flame kernel is assumed to expand spherically, its initial radius is converted into that of the equivalent-volume sphere, resulting in $r_i = (3V_i/4\pi)^{1/3}$.

The second stage is the early FK expansion, which is modeled relying on 1D mass, species, and energy conservation Eqs. [27] with the incorporation of temperature and reactant gradients at the outer flame surface derived from Yu and Chen's work on transient thermo-diffusion [28]. In this framework, the combustion is modeled as a one-step reaction process controlled by a deficient reactant A (e.g. fuel for lean mixtures) with mass fraction Y_A, while the pressure remains constant and uniform throughout the process. The flame front is treated as a vanishingly thin reactive spherical shell, with preheat and mass diffusion zones extending into the unburned mixture. The consideration of

temperature and reactant profiles, $T(r)$ and $Y_A(r)$ respectively, and the inclusion of transient thermo-diffusion enable capturing both linear and non-linear flame stretch effects with no need for external correlations, effectively superseding historical mass-and-energy kernel growth models [21]. Fig. 1 illustrates the FK model, including the temperature and deficient reactant profiles on the unburned mixture side.

To summarize the model, the kernel conservation laws are applied and rearranged, resulting in a system of two equations, i.e. Eqs. (2a) and (2b), where quantities related to the fresh mixture at flame temperature are denoted as $[\cdot]_{u,f} = [\cdot]_u(T_f)$ and those related to the burned gas as $[\cdot]_f$.

$$m_f c_{p,f} \frac{dT_f}{dt} = \left(\rho_u A_f S_L^0 \omega_f + \dot{m}_{en}\right)\left(h_{u,f} - h_f\right) + A_f k_{u,f} C_T \left.\frac{\partial T}{\partial r}\right|_{r_f} + P_e \tag{2a}$$

$$\frac{1}{Le}\left(\frac{k}{c_p}\right)_{u,f} C_A \left.\frac{\partial Y_A(v_f)}{\partial r}\right|_{r_f} = Y_{Au}\rho_u S_L^0 \omega_f \tag{2b}$$

Here S_L^0 is the planar adiabatic laminar flame speed, which burns at adiabatic temperature T_{ad}, while $\omega_f = \left(T_f/T_{ad}\right)^2 exp\left[-0.5\,T_a\cdot\left(T_f^{-1} - T_{ad}^{-1}\right)\right]$ accounts for the effect of a non-adiabatic flame kernel temperature, i.e. $T_f \neq T_{ad}$, on the reaction rate. P_e is the electric power supplied in arc/glow mode, and $\dot{m}_{en}$ is the entrainment mass flow rate, assumed proportional to P_e, which accounts for non-spherical flow effects induced by the electric discharge [30] [35]. Since the kernel surface area and mass can be expressed as $A_f = 4\pi r_f^2$ and $m_f = \rho_f \frac{4}{3}\pi r_f^3$, respectively, the system unknowns are the FK temperature, T_f, and its radius, r_f. However, these equations require the knowledge of temperature and deficient reactant gradients at r_f, which provide inherent estimation of flame stretch effects and are adapted from the results of transient thermo-diffusive theory [28] as follows:

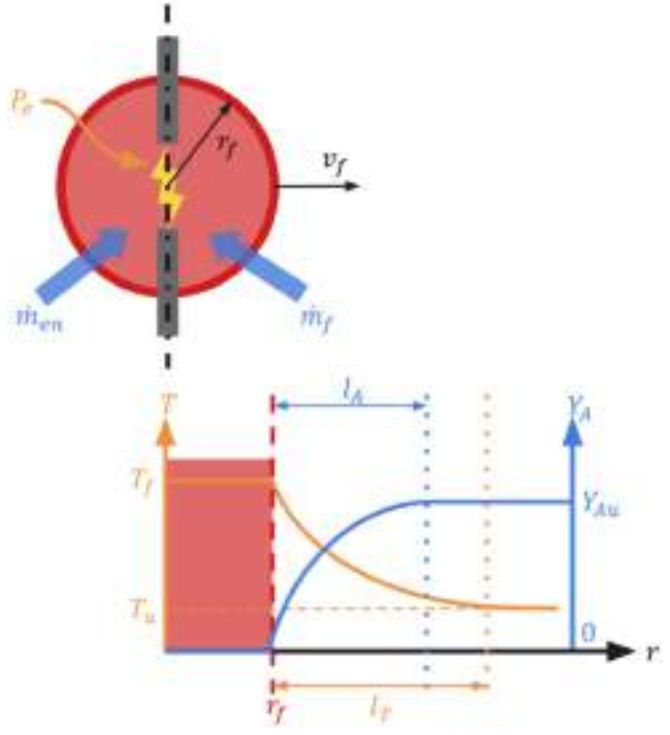

Fig. 1. Sketch of the flame kernel expansion model, including deficient reactant and temperature profiles outside the kernel.

$$\begin{cases} \left.\frac{\partial T}{\partial r}\right|_{r_f} = \left.\frac{\partial \theta}{\partial \phi}\right|_R \cdot \frac{(T_{ad} - T_u)}{l_T^0} = -\frac{f_{uT}}{R}\left[\theta_f + \theta_i(\vartheta(x) - 1)\right] \cdot \frac{(T_{ad} - T_u)}{l_T^0} \\ x = \exp\left(-\frac{\pi^2 {f_{uT}}^2}{R^2}\tau\right) \end{cases} \tag{3a}$$

$$\left.\frac{\partial Y_A}{\partial r}\right|_{r_f} = \left.\frac{\partial y_A}{\partial \phi}\right|_R \cdot \frac{Y_{Au}}{l_T^0} = \frac{f_{uY}}{R}\vartheta(x) \cdot \frac{Y_{Au}}{l_T^0},\ x = \exp\left(-\frac{\pi^2 {f_{uY}}^2}{LeR^2}\tau\right) \tag{3b}$$

The dimensionless terms in Eqs. (3a) and (3b) are defined in Eqs. (4) with respect to the planar adiabatic laminar flame and especially its absolute propagation speed $v_L^0 = (\rho_u/\rho_{ad})S_L^0$, which serves as the key point of reference. This approach accounts for the convective flows caused by thermal expansion, in contrast to purely thermo-diffusive models that assume no density jump across the flame.

$$\begin{aligned} &l_T^0 = \frac{k_{ad}}{\rho_{ad} c_{p,ad} v_L^0}, t_L^0 = \frac{l_T^0}{v_L^0}, R = \frac{r_f}{l_T^0}, \tau = \frac{t}{t_L^0}, U = \frac{dR}{d\tau} = \frac{v_f}{v_L^0} \\ &\phi = \frac{r}{l_T^0}, \theta = \frac{T - T_u}{T_{ad} - T_u}, y_A = \frac{Y_A}{Y_{Au}}, Le = \frac{(k/c_p)_{u,f}}{(\rho D_A)_f} \end{aligned} \tag{4}$$

Eqs. (3a) and (3b) are completed by Jacobi theta function $\vartheta(x) = 1 + 2\sum_{n=1}^{+\infty} x^{n^2}$ and by the definitions of f_{uT} and f_{uY}, given in Eqs. (5a) and (5b), respectively [27]:

$$f_{uT} = \left[\int_1^{+\infty} \frac{1}{s^2} \exp\left(-\frac{RU}{2}(s^2 - 1)\right) ds\right]^{-1} \tag{5a}$$

$$f_{uY} = \left[\int_1^{+\infty} \frac{1}{s^2} \exp\left(-\frac{LeRU}{2}(s^2 - 1)\right) ds\right]^{-1} \tag{5b}$$

Finally, in Eqs. (2) adjustment coefficients C_A and C_T account for the variation in thermodynamic properties caused by temperature and mixture composition, which is neglected by the thermo-diffusive theory. These coefficients can be calculated precisely only under two limiting scenarios, which are the adiabatic planar flame and the stationary flame ball, whereas for all other conditions the coefficients assume intermediate values. Limiting-scenario coefficients and values in intermediate conditions are found in the authors' previous work [27].

3. Input data for the flame kernel model

The FK model requires the knowledge of the thermochemical properties of the fuel/air mixture, as well as the ignition system characteristics. These input data are estimated according to the procedures and choices reported in the following subsections.

3.1. Evaluation of flame properties for different fuels

This section presents the estimation of the flame properties for two hydrocarbon fuels, methane and propane, and for hydrogen using software package Cantera, an open-source chemical kinetics solver [36]. As known, to characterize fully the flame properties of individual fuel/air mixtures a proper selection of the chemical reaction mechanism is required, and Table 1 reports detailed specifications of the mechanisms chosen for the investigated fuels.

For each fuel, the present calculation aimed to estimate a set of three parameters, namely the planar adiabatic laminar flame speed (LFS), S_L^0, the activation energy, E_a, and the mixture Lewis number. The calculation was conducted using a one-dimensional domain 1 cm long and discretized using 500 nodes to capture well the sharp species and temperature gradients. For the transport models, both the mixture-averaged and the much more demanding multicomponent formulations were

Table 1
Details of the kinetic mechanisms used for the cantera calculations.

Fuel	Kinetic mechanism	Mechanism characteristics	Reference
Methane, CH_4	GRI-Mech 3.0	5 elements, 53 species, 325 reactions	[37]
Propane, C_3H_8	San Diego	6 elements, 57 species, 268 reactions	[38]
Hydrogen, H_2	Zhang et al.	6 elements, 11 species, 32 reactions	[39]

tested, the latter also accounting for the Soret effect, but its inclusion led to minor differences only in the hydrogen LFS, consistently with the literature [40]. Therefore, to cover the wide range of operating conditions included in this work in a reasonable timeframe the much faster mixture-averaged model was applied.

Referring to the activation energy E_a, or the equivalent activation temperature $T_a = E_a/R_0$, with R_0 being the universal gas constant, the definition provided by Eq. (6) was used:

$$E_a = R_0 \cdot T_a = -2 \cdot R_0 \cdot \left[\frac{\partial ln(\rho_u S_L^0)}{\partial \frac{1}{T_{ad}}} \right]_{p,\phi} \tag{6}$$

being ρ_u the unburned gas density. The right-hand-side derivative was estimated as the angular coefficient of the linear regression of $ln(\rho_u S_L^0)$ against $1/T_{ad}$ obtained by altering the N_2-to-O_2 ratio of air by $\pm 0.5\%$ and $\pm$ 1%. Finally, for the Lewis number the formulation of Bechtold and Matalon was used [41], according to which an 'effective' Lewis number, Le_{eff}, is computed as a weighted average of the Lewis numbers of two reactants, as shown by Eqs. (7) to (9):

$$Le_{eff} = 1 + \frac{(Le_E - 1) + (Le_D - 1)\cdot\beta}{1 + \beta} \tag{7}$$

$$\beta = 1 + Ze\cdot(\varphi - 1) \tag{8}$$

$$Ze = \frac{E_a}{R_0}\cdot\frac{T_{ad} - T_u}{T_{ad}^2} \tag{9}$$

Here, Ze is the Zeldovich number, T_u is the unburned temperature, and Le_E and Le_D are the Lewis numbers of excess and deficient reactant, respectively. The reactants, fuel and oxygen, are associated alternatively with Le_E and Le_D based on equivalence ratio ϕ, and a similar relationship is valid for parameter φ. The values of φ, Le_E and Le_D are computed according to Eqs. (10) to (12) below:

$$\varphi = \begin{cases} \phi^{-1} & if\ \phi \le 1, \\ \phi & otherwise, \end{cases} \tag{10}$$

$$Le_E = \begin{cases} Le_{O_2} & if\ \phi \le 1, \\ Le_{fuel} & otherwise, \end{cases} \tag{11}$$

$$Le_D = \begin{cases} Le_{fuel} & if\ \phi \le 1, \\ Le_{O_2} & otherwise. \end{cases} \tag{12}$$

3.2. Validation of the flame properties

The present calculation procedure was applied to compute the E_a and Le_{eff} values for mixtures of the three aforementioned fuels with air, so as to perform a comparison with available literature data over a wide range of equivalence ratios [42–44]. This comparison is reported in Fig. 2 for ambient temperature and low pressures. It is immediately highlighted that the E_a calculation method outlined above struggles near the stoichiometric condition due to the lack of a clear difference between excess and deficient reactant, which leads to unphysical E_a peaks at $\phi \cong 1$. The solution to this issue, recommended in literature [43] and followed for all results in Fig. 2, is ignoring the E_a values computed in the $\phi = [0.8; 1.2]$ range and estimating them by interpolating the E_a obtained for leaner and richer mixtures.

For all the considered fuels, Fig. 2 shows that the experimental trends of both E_a and Le_{eff} are captured with acceptable accuracy by the simulations. For methane, Le_{eff} is reproduced quite well, whereas minor discrepancies emerge for E_a, which is underestimated by up to 15%

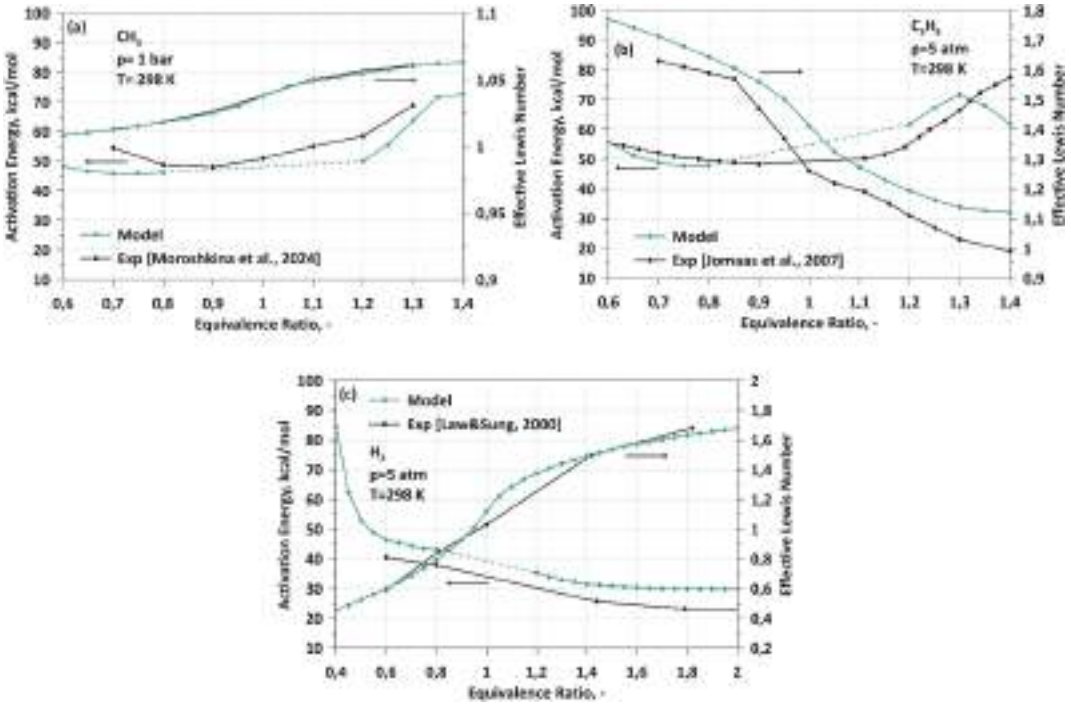

Fig. 2. Validation of activation energy E_a and effective Lewis number Le_{eff} for (a) methane, (b) propane, and (c) hydrogen. Dashed segments denote interpolated E_a (values)

away from the stoichiometric condition. For propane, the predicted Le_{eff} values overestimate the experimental outcomes by 5% to 10% going from lean to rich mixtures, while E_a is slightly overestimated in rich conditions. Finally, for the hydrogen-air mixture the modeled Le_{eff} agrees well with the reference values especially for lean conditions, while E_a is overestimated by about 10%.

The results in Fig. 2 can be considered an acceptable validation of the present calculation procedure, supporting its application to the prediction of both E_a and Le_{eff} over large ranges of pressure, unburned temperature, equivalence ratio, and inert gas ratios. Conversely to E_a and Le_{eff}, no validation for S_L^0 is included here, since it has already been conducted extensively by the authors who proposed the kinetic schemes used in this work.

3.3. Flame parameters and ignition system characteristics for the FK model application

The variability of operating conditions in SI engines requires that the flame parameters be computed for a wide range of mixture conditions. This was done using the procedure of Section 3.1 and expressing the results as maps of laminar flame speed S_L^0, activation energy E_a, and effective Lewis number Le_{eff}. Examples are shown in Fig. 3 to Fig. 5, which report for each fuel examined (CH_4, C_3H_8, and H_2) the isocontours of S_L^0, E_a, and Le_{eff} as a function of pressure and unburned temperature for a lean mixture ($\phi = 0.6$) with no inert gas ($x_r = 0$).

Looking at these figures, well-recognized literature trends of LFS are obtained for all fuels, i.e. S_L^0 values increasing with mixture temperature and decreasing with pressure (Fig. 3a, Fig. 4a, Fig. 5a). Concerning E_a, trends similar to those observed for S_L^0 are obtained for the two hydrocarbon fuels (CH_4 and C_3H_8 in Fig. 3b and Fig. 4b, respectively), whereas the activation energy of H_2 reported in Fig. 5b behaves very differently, being lowest at high temperatures and low pressures and highest at medium-to-high pressures and low temperatures. Finally, regarding Le_{eff}, the fuels show very different values under the same thermodynamic conditions due to their different diffusion characteristics. Indeed, Fig. 3c shows a near-unity Le_{eff} for methane over the entire pressure and temperature range explored, whereas in Fig. 4c propane has a $Le_{eff} \cong 1.6$ and slightly decreasing as the temperature increases. Conversely, lean hydrogen exhibits a Le_{eff} much lower than unity, with a decreasing trend as pressure rises (Fig. 5c). This case demands particular attention, because $Le_{eff} \ll 1$ is responsible for the onset of TD flame instabilities, as detailed in the following sections.

Finally, the ignition device considered in this work is an automotive ICE spark plug whose main characteristics are summarized in Table 2. The parameters were chosen consistently with the present FK model, with breakdown energy assumed proportional to unburned gas density (i.e. $E_{bd} \propto \rho_u$) following recent experiments [34]. Note that the values assigned to these parameters affect strongly both the ignition stage and the early FK expansion, with fading importance as the kernel grows larger.

4. Flame kernel duration

In this section, a kernel 'formation time' or 'duration' is extracted from the FK model of Section 2. In Section 4.1 a threshold is selected and applied to the FK model to define the kernel duration, whose response to different flame parameters and mixtures is examined in Section 4.2.

4.1. Definition and estimation of kernel duration

The FK model with the aforementioned input parameters was applied to compute the evolution of both flame radius r_f, and expansion speed v_f, for pressure/temperature levels (20 bar and 700 K) typical of an automotive ICE at the time of spark ignition. These outputs were calculated for different fuels, air/fuel ratios, and inert gas levels under the assumption of constant unburned pressure and temperature and ignoring any flame instabilities. As an example, Fig. 6 shows the evolution of r_f and v_f at two equivalence ratios (i.e. $\phi = 0.6$ and $\phi = 1.0$) and zero residual gas (i.e. $x_r = 0$) for the three fuels considered. For convenience, the elapsed time on the x-axis is converted into an equivalent crank angle degree (CAD) assuming an engine speed of 1000 rpm.

The solid lines in Fig. 6 refer to radius r_f, which increases almost linearly after a fast initial growth consistently with the trend of the dotted lines representing v_f, which, initially very high, decreases quickly until it approaches a constant value. This is due to the rapid drop in flame kernel temperature T_f that occurs when combustion replaces electricity as the main driver of the kernel expansion. Consequently, parameter ω_f, defined in Section 2 as a reaction rate correction term that accounts for a non-adiabatic temperature, also decreases, quickly reaching a close-to-unity value after which the flame expands at near-constant T_f and v_f. Here, the kernel has grown large enough that heat of combustion and thermal losses toward the unburned gas are almost balanced, and flame stretch plays a minimal role in influencing the expansion. In practical terms, the FK formation can be assumed to end when ω_f drops below a value marginally above 1, which means $T_f \cong T_{ad}$. This value, here denoted as $\omega_{f,end}$, is associated with final temperature $T_{f,end}$ and is set as follows:

$$\omega_{f,end} = \left(\frac{T_{f,end}}{T_{ad}}\right)^2 exp\left[-0.5\, T_a \cdot \left(\frac{1}{T_{f,end}} - \frac{1}{T_{ad}}\right)\right] = 1.1 \tag{13}$$

This condition is used to define a conventional time at which the kernel formation stage is completed, hereinafter referred to as kernel 'formation time' or 'duration'.

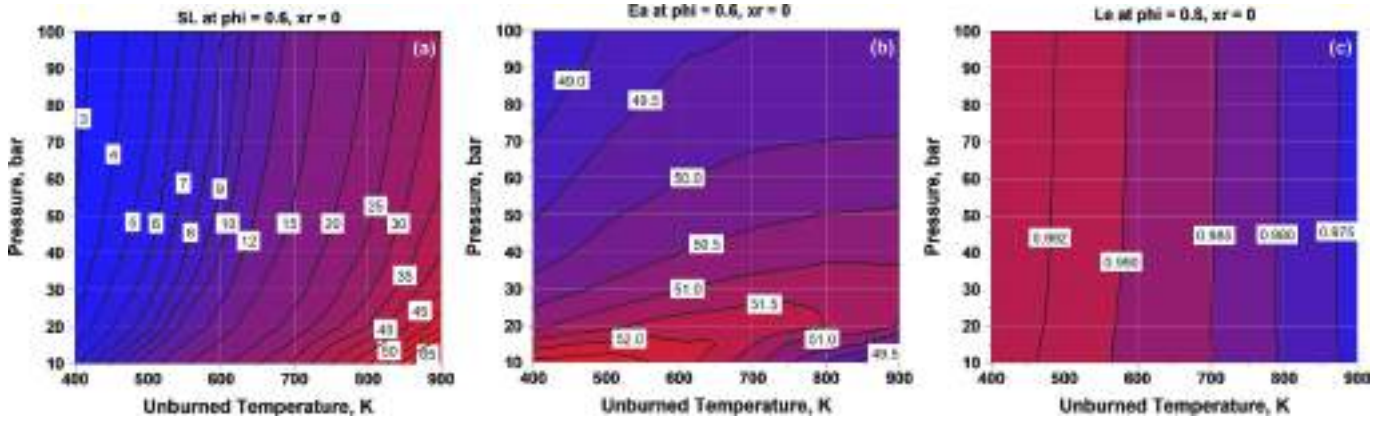

Fig. 3. Adiabatic laminar flame speed [cm/s] (a), activation energy [kcal/mol] (b), and effective Lewis number [−] (c) for methane at $\phi = 0.6$ and $x_r = 0$.

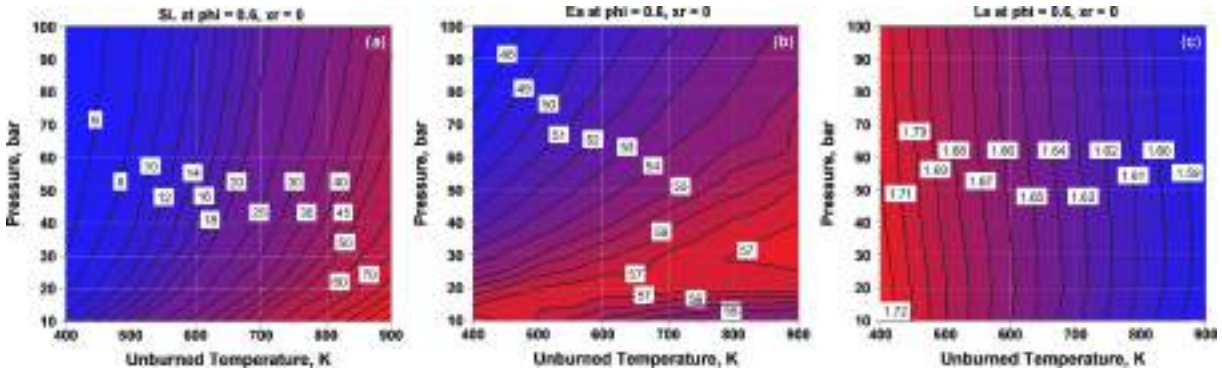

Fig. 4. Adiabatic laminar flame speed [cm/s] (a), activation energy [kcal/mol] (b), and effective Lewis number [−] (c) for propane at $\phi = 0.6$ and $x_r = 0$.

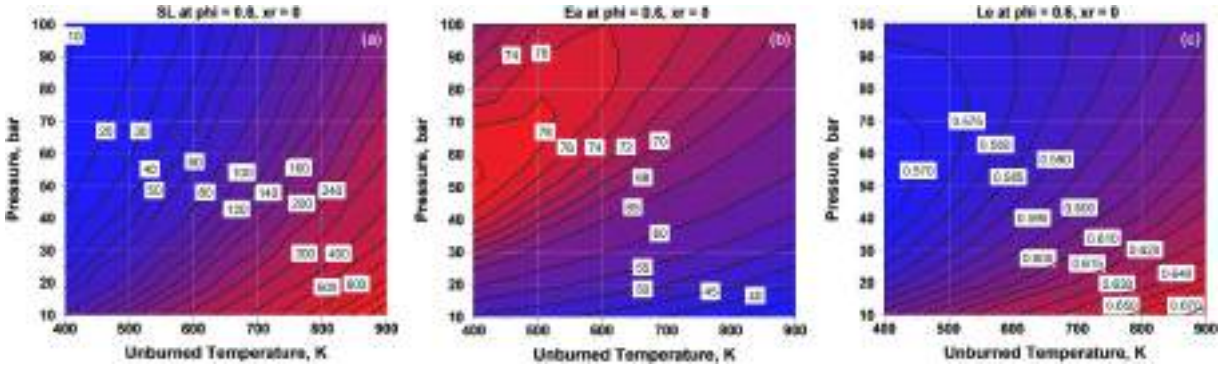

Fig. 5. Adiabatic laminar flame speed [cm/s] (a), activation energy [kcal/mol] (b), and effective Lewis number [−] (c) for hydrogen at $\phi = 0.6$ and $x_r = 0$.

Table 2
Main characteristics of ICE spark plug for application of the FK model.

Parameter and unit of measurement	Magnitude
Spark plug gap d_g, mm	0.6
Breakdown energy E_{bd}, mJ	[0.1; 10]
Breakdown efficiency η_{bd}, –	0.77
Electrical energy via arc/glow E_e, mJ	6
Arc/glow duration t_e, ms	0.3
Electrode gap efficiency η_g, –	1
Constant area for spark-driven mass flow entrainment C_d, mm^2	0.02

Following this definition, Fig. 6 shows that the kernel duration is shortest for hydrogen and longest for methane at the same ϕ, with propane in the middle. In addition, for a given fuel, the FK model reasonably predicts a kernel duration increase when moving from stoichiometric ($\phi = 1$) to lean mixtures ($\phi = 0.6$). Finally, it is noted that the final kernel radii for the three fuels (filled circles in Fig. 6) fall within the range [1.6; 2.0] mm using the threshold value of Eq. (13). Based on this observation, in the following subsection a radius of 2 mm is used as the threshold for evaluating the kernel duration as a function of the engine operating conditions.

4.2. *Effects of mixture conditions and flame parameters on kernel duration*

The effects of the key ambient thermodynamic variables on the kernel duration, expressed as a CAD interval for an engine speed of 1000 rpm, are highlighted in Fig. 7 for methane, propane, and hydrogen, covering the mixture conditions that typically occur in a SI engine around the ignition time. Each plot in Fig. 7 shows the change in kernel duration as a function of a single variable (temperature, pressure, equivalence ratio, or inert gas fraction) for fixed values of the other ones. The durations are expressed using a linear scale in Fig. 7a-b and a logarithmic scale in Fig. 7c-d.

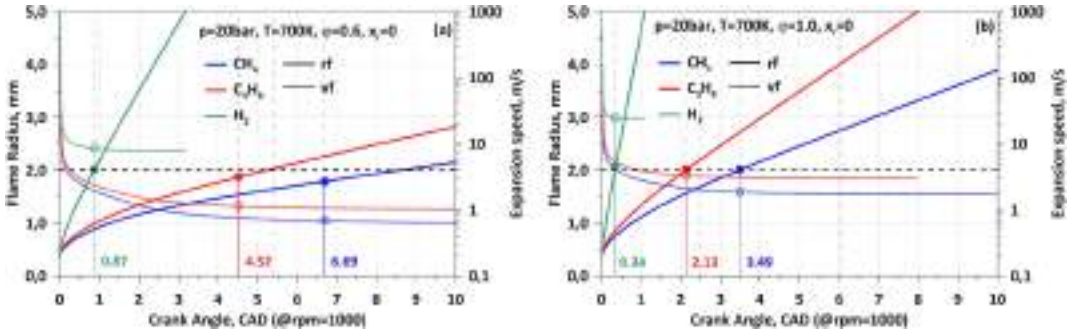

Fig. 6. Evolution of flame kernel radius r_f and speed v_f for methane, propane, and hydrogen at $\phi = 0.6$ (a) and $\phi = 1.0$ (b), and kernel durations based on Eq. (13) condition (filled and empty circles).

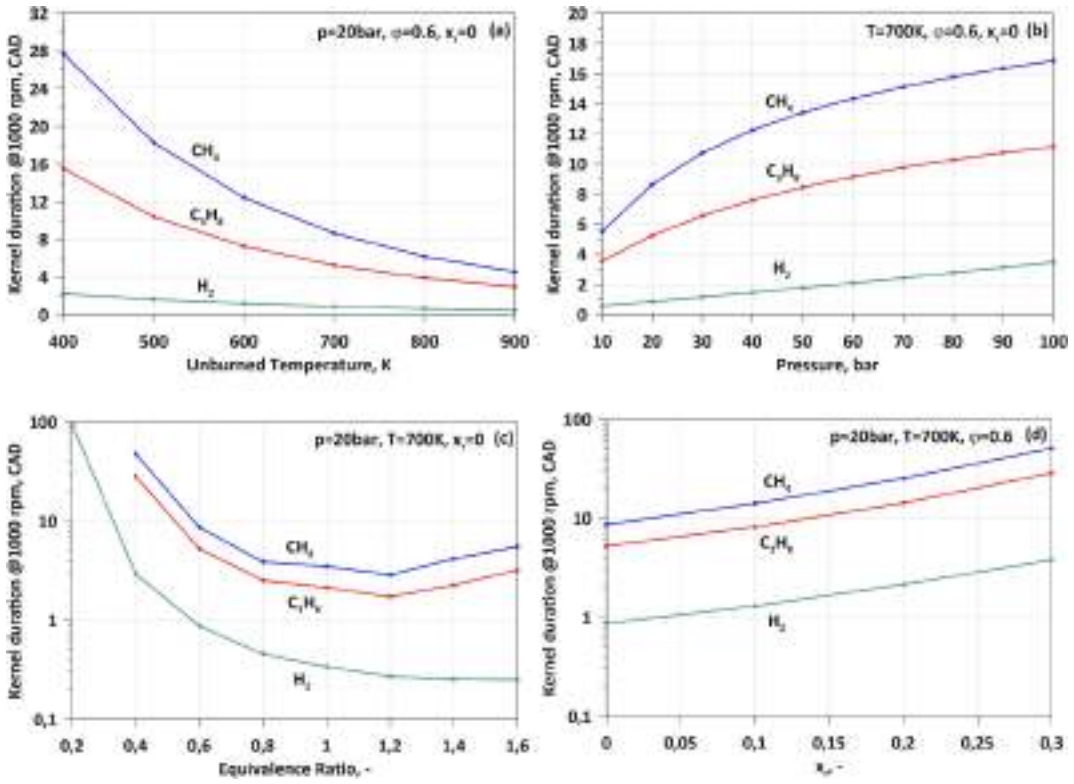

Fig. 7. Effects of unburned temperature (a), pressure (b), equivalence ratio (c), and inert gas fraction (d) on kernel duration at 1000 rpm for methane, propane, and hydrogen.

For all fuels, it is observed that the kernel formation time decreases with increasing temperature and increases as the pressure grows, with an inversely proportional trend to that of the LFS of each mixture. In Fig. 7c, the hydrocarbon fuels (i.e. CH_4 and C_3H_8) exhibit a minimum kernel duration for slightly rich mixtures ($\phi \cong 1.2$), which correspond approximately to those having highest LFS. Instead, for hydrogen a decreasing trend is observed in a wide range of ϕ until reaching a minimum value for the richest mixture considered here, $\phi = 1.6$. Fig. 7d shows an increase in kernel duration while raising the inert gas fraction for all fuels, which agrees well with the drop in the LFS values. These results highlight that hydrogen has a much shorter kernel duration than those of the two hydrocarbon fuels, which can even lead to effective misfires ($\Delta\theta \geq 30$ CAD) for very lean conditions ($\phi \leq 0.5$ in Fig. 7c) and highly diluted mixtures ($x_r > 0.25$).

Finally, emphasis on the kernel duration $\Delta\theta$ with ultra-lean hydrogen ($\phi = 0.4$) at the same ICE-like conditions is placed in Fig. 8, which shows the duration response to ±10% variations in the three flame parameters listed in Section 3, i.e. LFS S_L^0, activation energy E_a, and

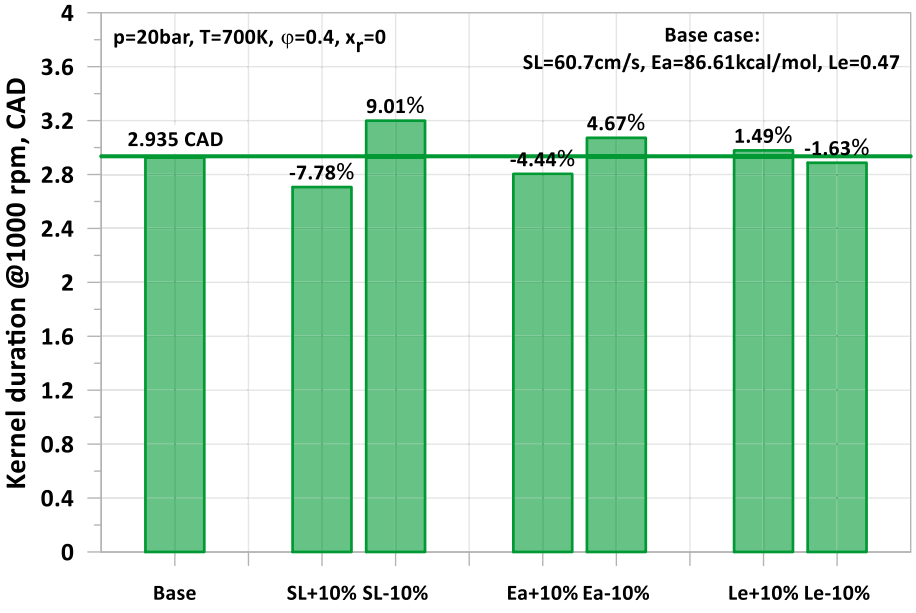

Fig. 8. Effect of ±10% variations in laminar flame speed, activation energy, and effective Lewis number on the kernel duration predicted using the present FK model.

effective Lewis number Le_{eff}. As depicted in Fig. 6, kernel duration $\Delta\theta$ should be roughly proportional to $1/S_L^0$, and this is confirmed by the first pair of bars in Fig. 8. The other two parameters influence the flame stretch as well, which is here positive and speeds up the kernel growth being $Le_{eff} \ll 1$. Since a stronger stretch is obtained increasing E_a and/or decreasing Le_{eff} [28], the duration should decrease accordingly with such variations. This is in fact the outcome reported in Fig. 8, which also shows that the sensitivities to ±10% variations in E_a and Le_{eff} are about 4.5% and 1.5%, respectively.

5. Application of the flame kernel model to the hydrogen SI engine

This section focuses on how the FK model is applied to estimate the early kernel growth in a hydrogen-fueled SI engine. Section 5.1 illustrates the inclusion of instability and turbulence into the FK model, while Section 5.2 describes the experimental investigation. Then, in Section 5.3 the experimental kernel durations are extracted and compared with those predicted using the FK model.

5.1. Effects of hydrogen flame instabilities and turbulence

As mentioned in Section 1, hydrogen/air flames are characterized by DL and TD instabilities, both of which increase the flame speed due to the enhanced mixing provided by the instability cells. However, as the impact of the DL instability can be neglected due to the sufficiently high pressures and temperatures inside the cylinder, only TD effects are considered here. Additionally, the TD cells can interact with the turbulent flow field, ultimately exerting synergistic effects on the flame speed. This combination generates a turbulence-affected unstable flame speed, S_S, which effectively replaces the LFS, hereinafter generalized to S_L, in all the FK model calculations.

With regard to the estimation of the effects caused by both TD instability and turbulence, the approach proposed by Howarth et al. [30] was adopted in this work. This approach is based on an instability parameter, ω_2, expressed by Eq. (14) as a function of effective Lewis, Prandtl ($Pr = \mu c_p/k$, with μ dynamic viscosity, c_p specific heat at constant pressure, and k thermal conductivity), and Zeldovich (Ze as defined in Eq. (9)) numbers through coefficients $B_{j=1,2,3}$ computed according to Altantzis et al. [45]:

$$\omega_2 = -\left[B_1 + Ze\cdot\left(Le_{eff} - 1\right)\cdot B_2 + Pr\cdot B_3\right] \tag{14}$$

Positive values of ω_2 identify the presence of TD instabilities, whose effects on the increase of the flame speed with respect to the LFS vary depending on the pressure regime. TD instabilities magnitude, expressed as the ratio between unstable flame speed S_F and S_L, is quantified as follows:

$$\frac{S_F}{S_L} = \begin{cases} \exp(0.08\cdot\omega_2) & if \quad \Pi \le \Pi_{crit}, \\ 1 + 0.47\cdot\omega_2 & otherwise, \end{cases} \tag{15}$$

where $\Pi = p\,[kPa]/101.3$ is the normalized mixture pressure, to be compared with the critical value, Π_{crit}, given by Eq. (16) as a function of ϕ and normalized temperature $\Theta = T\,[K]/300$:

$$\Pi_{crit} = \left(\frac{20\cdot\phi}{7 - 2\cdot\Theta}\right)^{\frac{150}{(21+10\cdot\Theta)}} \tag{16}$$

According to Eq. (15), stronger TD effects are generally obtained when Π exceeds its critical level, while $\omega_2 \le 5$ in typical conditions of ICEs operated with lean hydrogen mixtures.

Finally, the interaction between TD cells and turbulent eddies leads to a further increase in the flame speed, expressed by the ratio between 'effective' turbulence-affected unstable flame speed S_S and unstable flame speed S_F. This ratio is estimated according to Eq. (17):

$$\frac{S_S}{S_F} = 1 + 0.26\cdot c_{Ka}\cdot exp(-0.038\cdot\omega_2)\cdot\sqrt{Ka} \tag{17}$$

where c_{Ka} is a tuning constant and Ka the Karlovitz number, computed by Eq. (18):

$$Ka = \left(\frac{l_T}{\eta}\right)^2 \tag{18}$$

where l_T is the flame thickness and η is the Kolmogorov length scale. In particular, Eq. (17) indicates that the presence of small-scale turbulent eddies magnifies the flame instability effects through $\sqrt{Ka}$, but also that this impact becomes smaller as the instability level rises, which is expressed through the exponential coefficient decreasing as ω_2 increases. The effective flame speed, S_S, is the quantity that replaces S_L in the FK model when applied to turbulent lean hydrogen flames.

5.2. Engine system, operating conditions, and preliminary 3D CFD analysis

The hydrogen engine used for the present experimental investigation is a single-cylinder SI research unit mounted on a test cell located in the ICE Laboratory of the CMT - Clean Mobility & Thermofluids Research Institute in Valencia (Spain). The main engine characteristics are listed in Table 3, while the layout of the experimental test cell is illustrated in Fig. 9.

The single-cylinder SI engine in Fig. 9 has two intake valves and two exhaust valves. The orientation of the intake ducts, the geometry of the combustion chamber, and the valve arrangement promote the generation of a tumble motion during the intake stroke. The engine is equipped with a gaseous hydrogen injector on the intake side, and an external compressor is used to provide sufficiently high intake pressure to allow operation with lean mixtures. The experimental apparatus includes also several sub-systems for the control and measurement of all operating variables. The intake pressure and temperature are controlled via an external screw compressor and an air heat exchanger, respectively, while the exhaust back-pressure is adjusted using a knife-gate valve mounted along the exhaust pipe. The hydrogen, stored in a pressurized tank, is metered by a dedicated control system, and its pressure is properly reduced before being fed to a Zavoli JET port injector, specifically designed for gaseous fuels with a maximum operating pressure of 4.5 bar and a temperature range of −40 to 120 °C. As for the measurement devices, a Bronkhorst F-113 AC flow meter is used for the hydrogen mass flow rate, while the volumetric flow rate of air is measured using a Kromschröder meter. Multiple piezoresistive sensors collect the average intake/exhaust pressures, while a high-frequency piezoelectric transducer is used to collect the in-cylinder pressure trace. The continuous acquisition of NO_x emission levels is performed by a HORIBA MEXA-7600EGR gas analyzer. An overview of measured parameters, measuring devices, and their accuracy is provided in Table 4.

Within a single test, the measured data include key engine performance parameters (torque, speed, etc.), NO_x emissions, and in-cylinder pressure traces for 250 consecutive cycles. The combustion stability is

Table 3
Key data on the engine used for the present experimental investigation.

Variable	Type or value
Engine type	Single-cylinder SI unit
Fuel type	Hydrogen
Displacement	454.2 cm^3
Bore x Stroke	82 mm × 86 mm
Compression ratio	10.7
Nr. of valves per cylinder	4
Intake valve opening/closing @ 0.2 mm lift	8 CAD BTDC / 30 CAD ABDC
Exhaust valve opening/closing @ 0.2 mm lift	38 CAD BBDC / 21 CAD ATDC
Injection system	Port fuel injection
Engine boosting	External compressor

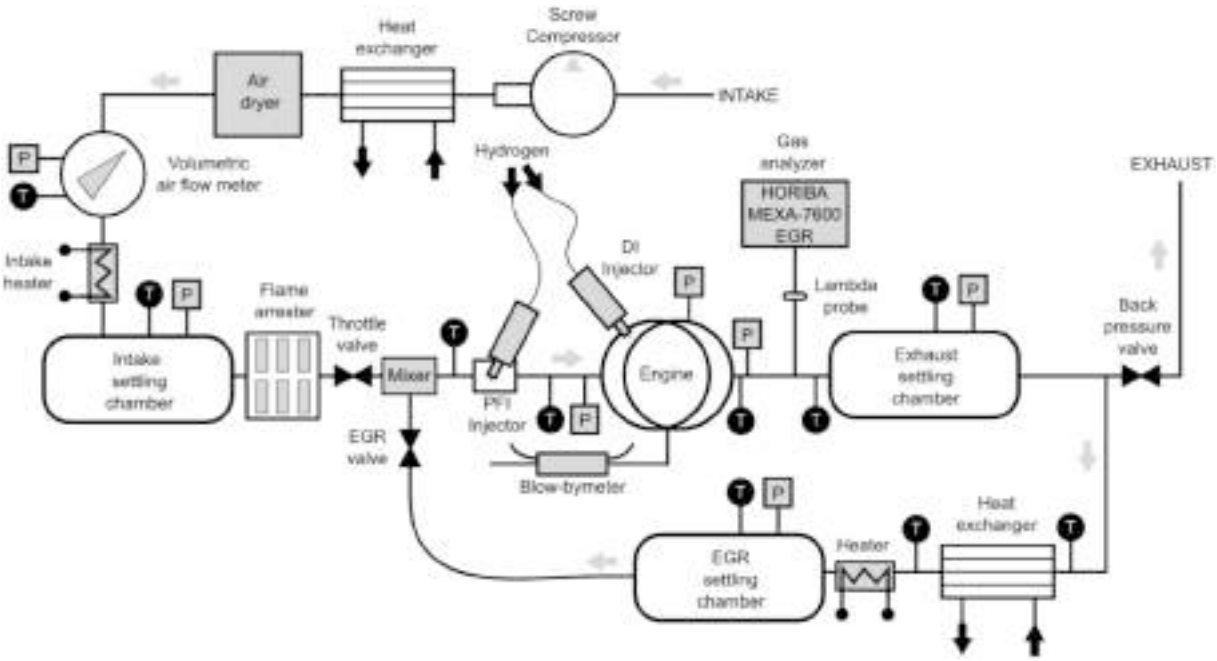

Fig. 9. Schematic diagram of the experimental test cell.

Table 4
Measured variables, engine sensors, and related accuracy.

Parameter (low frequency)	Sensor type	Measuring range	Accuracy
Engine speed	Optical angular encoder	1–6000 rpm	±1 rpm
Engine torque	Strain gauge	−200 – 200 Nm	±1 Nm
Air mass flow	Air flow meter	0.6–100 m^3/h	±1%
Hydrogen mass flow	Thermal flow meter	200–1600 l/min (based on N_2)	±0.5%
Fluid temperature	Pt100 thermoresistance	-200-850 °C	±0.3 °C
Intake pressure	Piezoresistive transducer	0–10 bar	±1%
Exhaust pressure	Piezoresistive transducer	0–10 bar	±0.3%
Intake temperature	Type K thermocouple	0–1000 °C	±0.5 °C
Exhaust temperature	Type K thermocouple	0–1000 °C	±0.5 °C
Parameter (high frequency)	**Sensor type**	**Measuring range**	**Accuracy**
In-cylinder pressure trace	Piezoelectric transducer	0–250 bar	±0.3% linearity
Intake pressure	Piezoresistive transducer	0–10 bar	±0.001 bar
Exhaust pressure	Piezoresistive transducer	0–10 bar	±0.001 bar
Pollutant emissions	**Sensor type**	**Measuring range**	**Accuracy**
NO_x concentration	HORIBA MEXA-7600EGR gas analyzer	0–10 kppm	±3%

Table 5
Engine operating points investigated in the present work (1500 rpm fixed rotational speed).

Case, #	Equivalence ratio ϕ, –	Spark timing, CAD AFTDC	Plenum pressure, bar	BMEP, bar
1	0.71	−2.0	0.76	3.18
2	0.63	−4.2	0.83	3.37
3	0.56	−8.0	0.90	3.46
4	0.50	−12.2	0.97	3.54
5	0.45	−16.2	1.04	3.60
6	0.42	−20.0	1.12	3.57
7	0.39	−20.0	1.18	3.65
8	0.36	−24.2	1.27	3.65
9	0.34	−28.2	1.35	3.65
10	0.31	−30.2	1.41	3.65
11	0.29	−32.0	1.48	3.62
12	0.28	−32.0	1.54	3.54
13	0.26	−36.2	1.61	3.43
14	0.25	−36.2	1.67	3.18
15	0.42	−24.2	1.79	6.61
16	0.38	−26.0	1.90	6.50
17	0.37	−28.2	2.00	6.75
18	0.33	−32.0	2.15	6.83
19	0.31	−34.2	2.27	6.81
20	0.30	−36.2	2.35	6.75
21	0.39	−30.2	2.48	8.05

monitored by evaluating the cycle-to-cycle variation through the coefficient of variation of IMEP (CoV_{IMEP}), and the stability of the tested operating condition is considered acceptable if CoV_{IMEP} is below 5%. More detailed information is provided in a recent dedicated paper [46].

Concerning the present experimental campaign, the engine was operated at a fixed speed of 1500 rpm to investigate the 21 operating points (OPs) reported in Table 5 and selected to emulate the typical operating conditions of an equivalent multi-cylinder engine mounted on a vehicle performing a real-world driving cycle. The OPs cover a broad interval of equivalence ratios ϕ, from 0.25 to about 0.70, combined with a wide spanning of the spark timing from about −36.0 CAD up to −2.0 CAD AFTDC. Three load levels were explored, i.e. about 3.3, 6.5, and 8.0 bar BMEP, and for the lower loads the rise in the mixture leaning was compensated by an increase in the intake plenum pressure. A dedicated error analysis was conducted on the experimental outputs following a literature methodology [47].

Following the experimental tests, a preliminary 3D CFD analysis was carried out to obtain information about flow and turbulence intensities for the investigated SI engine. The CFD simulation was performed using the CONVERGE software [48] and considering a computational domain composed of the engine cylinder and portions of the intake/exhaust ports. A hexahedral grid with a base cell size of 4 mm was adopted, with specific mesh refinements near solid surfaces and valves and an adaptive mesh refinement (minimum cell size of 0.125 mm) to increase the grid resolution in domain regions with high temperature and velocity

gradients. The numerical solution was achieved using an unsteady Reynolds-averaged Navier-Stokes approach and a *k-ε* turbulence model. All details on the 3D model setup are presented in a dedicated paper [49], where the results are validated against experimental data. The simulation was conducted under motored conditions at 1500 rpm to extract the variations of in-cylinder mass-averaged turbulence intensity, u', and integral length scale, L_i, with the crank angle, as shown in the example of Fig. 10. From these results, both u' and L_i were derived at the spark timing and then passed as input parameters to the FK model, which was applied to estimate the kernel duration for each of the 21 OPs considered.

5.3. Experimental kernel durations against FK model predictions

This section describes the methodology adopted to estimate the combustion delays of all the 21 OPs with respect to the spark-ignition event. This delay is defined here as the experimentally detected time interval between the spark ignition and the instant when combustion starts influencing the in-cylinder pressure. The experimental delays are compared with the kernel durations predicted by the FK model according to the indications laid out in Section 4.

The experimental combustion delay was estimated with a three-pressure analysis (TPA) of the mean pressure cycles measured in the cylinder and near the intake and exhaust ports. A thermodynamic two-zone inverse model provided the experimental burn rate and hence enabled finding the CAD associated with the start of combustion (SoC), here identified as the crank angle where the burn rate exceeded $3.4{\cdot}10^{-3}$mg/CAD, an arbitrary threshold selected as suitable for the present SI engine and test equipment. As an example, Fig. 11 shows the TPA results for four OPs, namely cases #4, #12, #15 and #19, highlighting that the SoC lagged behind the spark timing (ST) by very different CAD intervals. An additional confirmation of the actual SoC was obtained by considering the second derivative of the mean in-cylinder pressure trace. Indeed, the SoC could be equally identified as the point where a local minimum in the second derivative of the pressure occurred due to the combustion onset. All the cases plotted in Fig. 11 confirm the validity of this method, showing that the crank angles at which the second derivative of the pressure started rising abruptly (red circles in Fig. 11) correspond to the SoC angles identified by the inverse analysis.

This analysis enabled quantifying also the experimental combustion delay, measured as the difference between SoC and ST. This is plotted in red in Fig. 12 for all the 21 OPs, together with the respective ϕ values, shown in black. The results indicate that the combustion delays increased as ϕ fell, but the values hardly exceeded 15 CAD. The longest delay, around 20 CAD, was recorded for case #14, which exhibits the lowest equivalence ratio ($\phi = 0.25$). Fig. 12 reports also the kernel durations, predicted either neglecting or considering the effects of turbulent TD instabilities and represented with dashed and solid blue lines, respectively. Interestingly, for the leaner OPs the FK model predictions without instability completely disagree with the experimental delays, leading to kernel durations exceeding 50 CAD. Conversely, the FK durations predicted accounting for the TD instability are in much better agreement with the measured delays across the entire dataset, the average error being about 1.5 CAD. In some OPs, such as #19, the concordance is also due to a favorable change in the pressure regime of the TD sub-model ($\Pi > \Pi_{crit}$), which led to a stronger instability that sped up the kernel growth.

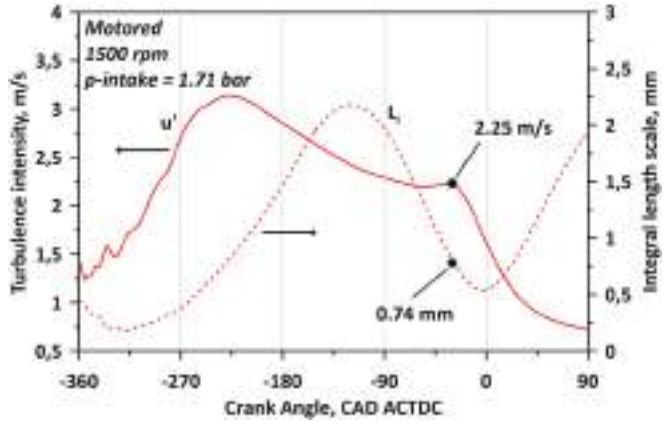

Fig. 10. Turbulence intensity, u′, and integral length scale, L_i, as a function of CAD at 1500 rpm for motored engine conditions and specified intake pressure.

The comparison in Fig. 12 cannot be considered a rigorous validation of the FK model, since the two sets of results depend on arbitrary choices (threshold for ω_f in the FK model and minimum burn rate in the experimental data). However, considering also the scarcity of literature data on the FK growth in hydrogen-fueled SI engines, the widespread agreement between experimental combustion delays and predicted FK durations strongly supports the reliability of the selected criteria, which may possibly extend to SI engines with similar geometry (e.g. similar unitary displacement). Therefore, the predicted FK durations were assimilated to the actual delays between ST and SoC. Upon reaching the SoC, the simulation was switched to the 0D/1D engine model for prediction of in-cylinder combustion, engine performance, and NO_x emissions as described in the following section.

6. Modeling and validation of the overall combustion process

In this section, the SI combustion after the FK formation is finally investigated. Section 6.1 presents the 0D sub-models implemented in GT-Power™ to complete the combustion modeling and estimate the engine-out NO_x emissions, thus closing the 0D/1D simulation. In Section 6.2, the model outcomes with and without FK durations are compared with their experimental counterparts, showing the ability of the proposed modeling framework to replicate the key engine performance and emission outputs.

6.1. Modeling of turbulence effects and NO_x emissions

The turbulent combustion process occurring in the engine cylinder was reproduced by adopting the fractal combustion model [50]. This applies properly in the wrinkled / corrugated flamelet combustion regimes and assumes that chemical kinetics and turbulence phenomena can be decoupled in such a way that the effect of the turbulent eddies is only to wrinkle the laminar quasi-spherical flame surface, which continues to propagate at the local (stretched) flame speed. This speed is usually the LFS, but effective flame speed S_S is used here to account for TD instability. This leads to the turbulent burning rate formulation in Eq. (19), which includes a larger flame area, A_T, compared to the laminar one, A_L, due to the flame wrinkling:

$$\left(\frac{dm_b}{dt}\right)_{turb+TD} = \rho_u{\cdot}A_T{\cdot}S_S = \rho_u{\cdot}A_L{\cdot}S_S{\cdot}\left(\frac{A_T}{A_L}\right) = \rho_u{\cdot}A_L{\cdot}S_S{\cdot}c_\Sigma\,\Sigma \tag{19}$$

The flame wrinkling factor, Σ, is evaluated according to Eq. (20):

$$\Sigma = \left(\frac{L_{max}}{L_{min}}\right)^{D_3-2} \tag{20}$$

where the fractal dimension, D_3, and minimum and maximum flame wrinkling scales, L_{min} and L_{max} respectively, were computed using a phenomenological 0D *K-k-T* turbulence sub-model [51]. As mentioned above, this burn rate formulation already takes into account the hydrogen TD instabilities by replacing the LFS, S_L, with the effective flame speed, S_S, but an additional correction is necessary for the large-scale turbulence [52]. This is the purpose of term c_Σ in Eq. (19), which acts as a correction factor for the fractal model due to the

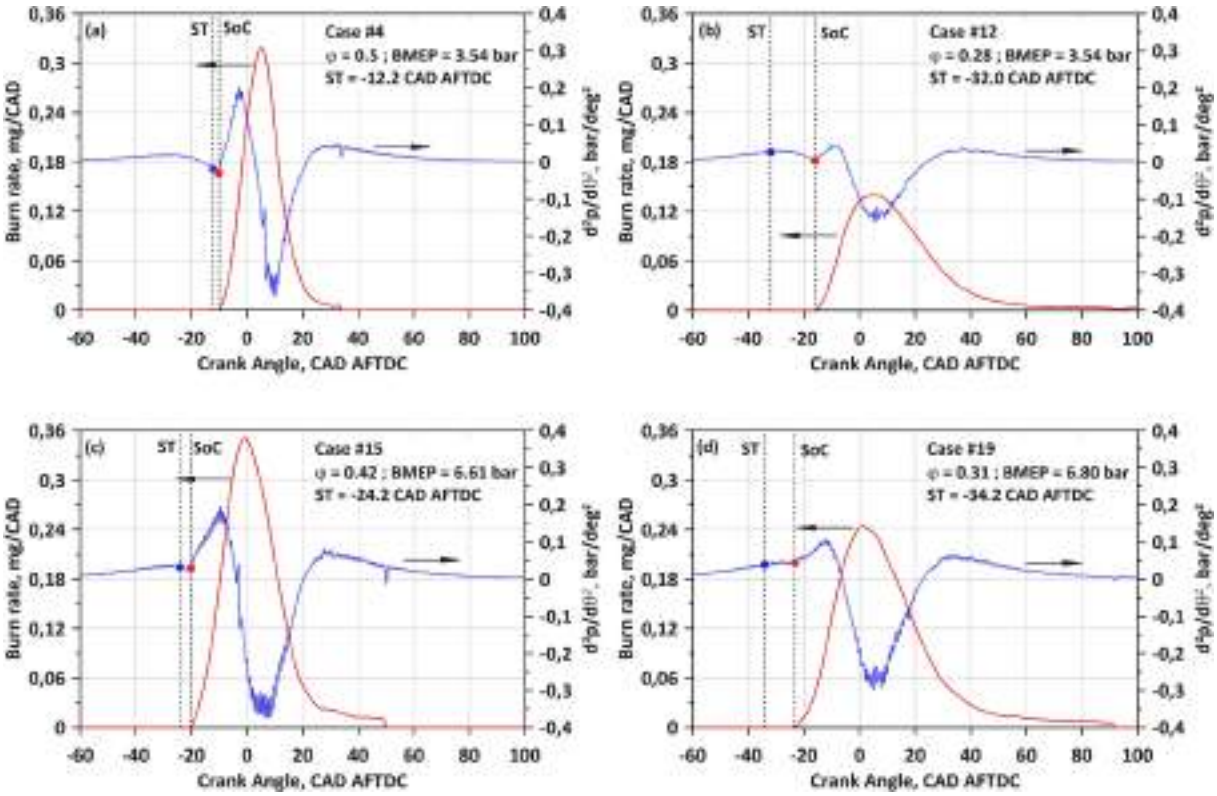

Fig. 11. Identification of the angular delay between ST and SoC from experimental pressure cycles: (a) case #4, (b) case #12, (c) case #15 and (d) case #19. The burn rates from TPA are plotted in red, and the second derivatives of pressure in blue. (For interpretation of the references to colour in this figure legend, the reader is referred to the web version of this article.)

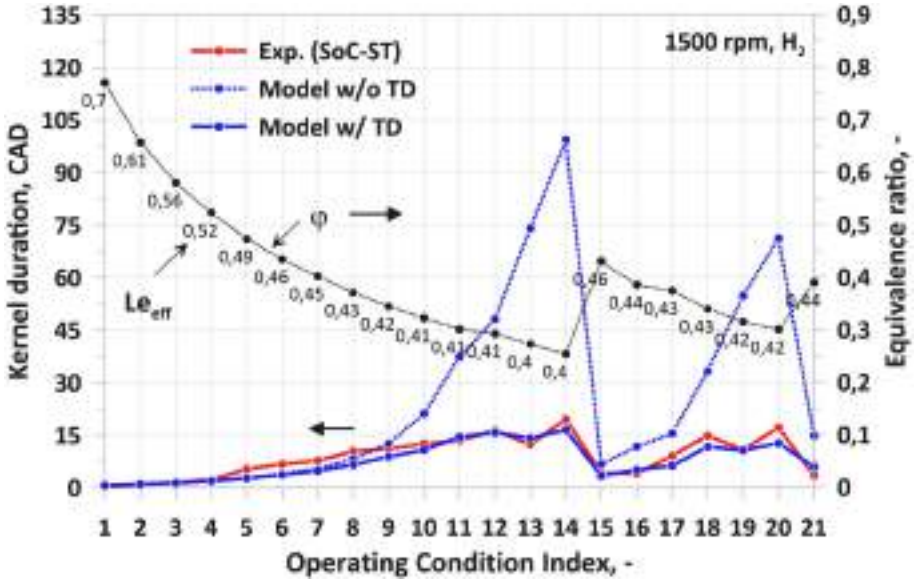

Fig. 12. Comparison between experimental angular delays between ST and SoC and kernel durations predicted by the kernel model with (w/) and without (w/o) TD effects for all 21 engine OPs.

combustion regime changing from wrinkled / corrugated flamelets to thickened flames when Karlovitz number $Ka \geq 1$. The overall behavior of c_Σ is reported in Eq. (21), while its full expression is provided in the original paper [52].

$$c_\Sigma = \begin{cases} 1 & \text{if } Ka < 1, \\ f(Ka) > 1 & \text{otherwise.} \end{cases} \tag{21}$$

The combustion model is closed with two modifications to the formulation of the burning rate. The first one is introduced to handle the transition from an initial quasi-laminar burning regime, where $\Sigma = 1$, to a fully developed turbulent flame propagation, whereas the other one modulates the transition from the fully developed turbulent flame propagation to the wall combustion, where the propagation reverts to laminar conditions. These modifications are discussed in detail in a

previous paper by the present authors [53].

The in-cylinder combustion model was activated upon reaching the predicted FK duration, i.e. at the modeled SoC that corresponds to the CAD interval after ST reported in Fig. 12. The calculation proceeded until either the combustion was completed or the exhaust valves were opened.

Concerning the NO_x emissions, a dedicated sub-model was used to estimate the NO_x levels caused by the high combustion temperatures. A multi-zone approach in the burned gas region was applied to account for the thermal stratification, which resulted in higher-temperature zones near the ignition site and colder zones close to piston head and cylinder walls. The NO formation was estimated using the solution proposed by Lavoie et al. [54], who simplified six elementary reactions (three for the extended Zeldovich mechanism and three for the intermediate N_2O one) into an equivalent one-step reaction. This reaction was applied separately to each burned gas parcel, cumulating the individual concentrations into a single one upon the opening of the exhaust valves.

6.2. Assessment of predicted combustion rates, engine performance, and NO_x emissions

The 0D/1D engine simulation model was initially applied to model the in-cylinder combustion for the entire dataset in Table 5 without considering any combustion delay between ST and SoC. The computation was conducted by running 30 engine cycles to let the simulation converge to a steady state, after which the final cycle was taken as the model output. Fig. 13 shows the comparison between model predictions and experimental results in terms of in-cylinder pressure trace and burn rate in OPs #4, #12, #15 and #19. The first two OPs are representative of low engine loads, while the other two refer to medium-load cases, with substantial differences in equivalence ratios and spark timings. Looking at the model predictions, plotted in blue in Fig. 13, it is clear that the modeled SoC angles do not reproduce the test data correctly, leading to combustion onsets that always precede their experimental counterparts. Furthermore, the combustion onset error increases as the equivalence ratio decreases, resulting in a progressively anticipated heat release that causes a faster growth of the in-cylinder pressure and a higher pressure peak (Fig. 13a-d).

The significant deviations between model and experimental results observed in Fig. 13 highlight the need for a kernel formation time in the computational procedure. This can be provided by the kernel duration (= combustion delay) predicted by the present FK model and shown in Fig. 12 for the 21 OPs considered in this work. Once included in the 0D/1D engine model, this delay resulted in the pressure and burn rate plots of Fig. 14.

The results in Fig. 14 show that the application of the FK model for estimating the SoC—ST delay significantly improves the combustion onset prediction for the same set of engine OPs considered in Fig. 13. The improved SoC prediction leads to a much better agreement between simulated and experimental traces of in-cylinder pressure and burn rate, reproducing well their overall trends, peak locations, and intensities. Of particular note is the good outcome achieved for the ultra-lean case #12 ($\phi = 0.28$), since at similar equivalence ratios a CFD-based simulation recently conducted by some of the present authors yielded unsatisfactory results [49].

This comparison shows that, with ultra-lean hydrogen/air mixtures ($\phi \leq 0.5$), the quality of the present SI engine simulation comes from both an accurate prediction of the FK formation time and a reliable estimation of the TD instability effects on the burning rate throughout the entire combustion process. However, the addition of the ST-SoC delays resulted in a higher computational effort, with the total processing time for a single OP rising from 1 to 2 min to 4–5 min on a modern small desktop workstation. This increase was caused by the integral terms in Eqs. (5a) and (5b), whose calculation takes a few seconds for each engine cycle computed to simulate a single OP.

In the final step, the calculation was extended to all the 21 OPs, resulting in the outcomes reported in Fig. 15. Firstly, Fig. 15a compares the predicted SoC and characteristic combustion angles MFB_{10}, MFB_{50}, and MFB_{75} with those obtained from the TPA. For these main combustion events, a good overall agreement between model results and experimental data is observed, although moderate prediction errors occur for both MFB_{10} and MFB_{50} especially in OPs #11 to #13, which refer to very low ϕ. For these cases the burning rate appears slightly underestimated, which could imply changes in the flame regime related

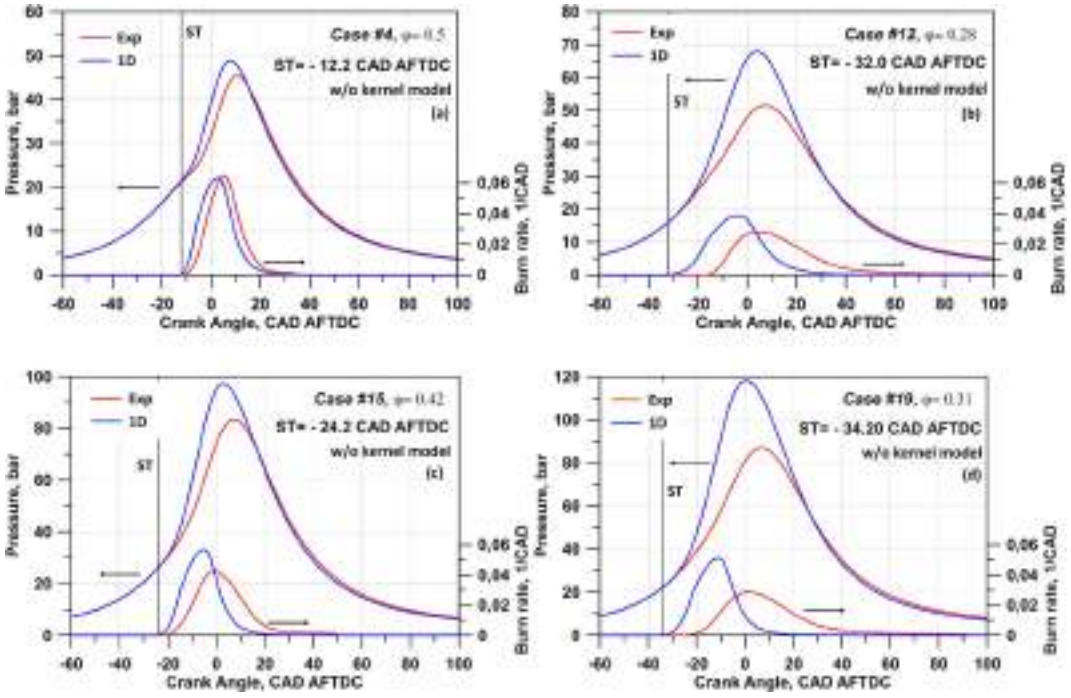

Fig. 13. Comparison of experimental (Exp) traces of in-cylinder pressure and burn rate with predicted (1D) traces without the FK model in four OPs: (a) case #4, (b) case #12, (c) case #15, and (d) case #19.

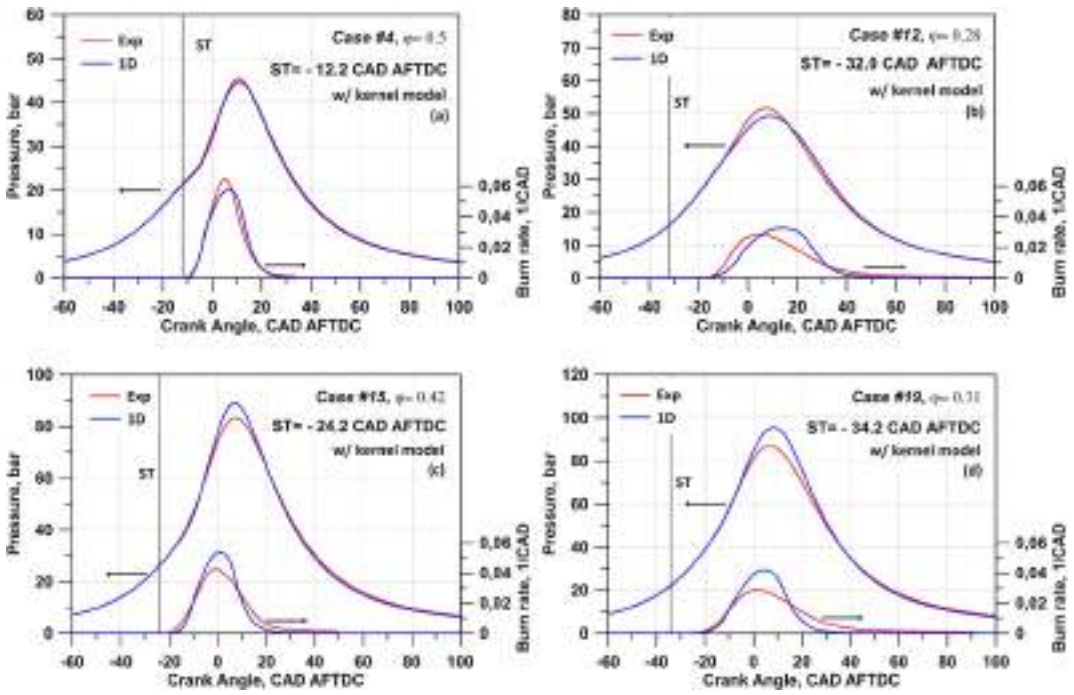

Fig. 14. Comparison of experimental (Exp) traces of in-cylinder pressure and burn rate with predicted (1D) traces using the FK model in four OPs: (a) case #4, (b) case #12, (c) case #15, and (d) case #19.

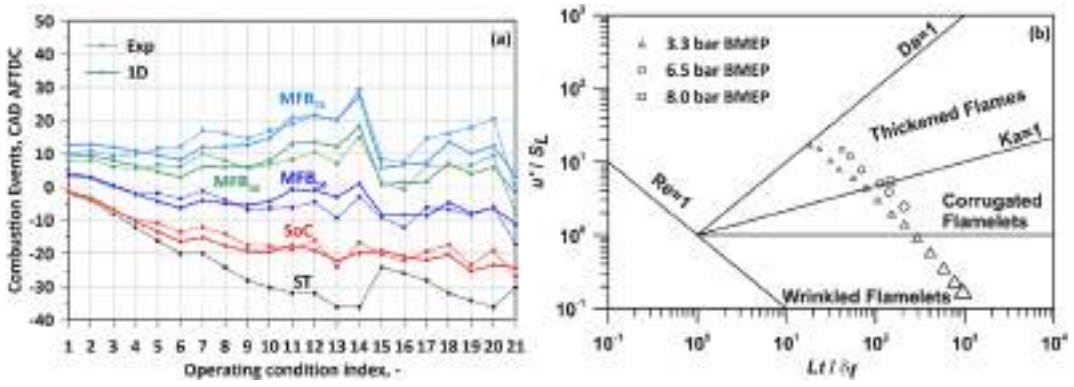

Fig. 15. Comparison between experimental data (Exp) and model predictions (1D) for the main combustion events (a), and Borghi diagram with symbols referring to characteristic velocity and length scale ratios in the combustion center, MFB_{50}, with symbol size proportional to the equivalence ratio (b).

to the Karlovitz number that were not fully captured by the adopted sub-model. Additionally, several higher-load OPs (OPs #17, #19, and #20) exhibit some prediction errors in the combustion tails, with the model underestimating the experimental MFB_{75} angles. These discrepancies may again depend on a combustion regime change not adequately captured, but they may also derive from a too simplified modeling of the flame-wall interaction.

A clearer light on the role of the combustion regime is shed by Fig. 15b, which reports the Borghi diagram hosting, for all 21 OPs, the modeled ratios of characteristic length and velocity scales at the combustion center, MFB_{50}. To distinguish the operating conditions, the symbol sizes are proportional to the ϕ values listed in Table 5. It is noted that for the low-load OPs (3.3 bar BMEP), as the mixture gets leaner the combustion regime moves from the wrinkled flamelets ($\phi \geq 0.44$) through the corrugated flamelets ($0.34 \leq \phi < 0.44$) to the thickened flames ($\phi < 0.34$). A similar trend occurs for the points at 6.5 bar BMEP, while the OP at 8.0 bar BMEP borders the thickened flames regime. These outcomes confirm that the slightly higher modeling errors observed above are associated with this regime, suggesting that the estimation of the corrective factor c_Σ used in Eq. (19) could be improved. Nevertheless, the 0D/1D engine model as currently proposed captures quite reliably the overall combustion development, yielding acceptable results for all 21 OPs.

Turning the attention to the engine outputs, Fig. 16a reports the assessment of the engine BMEP for all 21 OPs, showing that a satisfactory agreement is achieved between model predictions and experiments. The low average error, of about 5.3%, results from the reliable simulation of several overlapping effects, including cylinder filling, in-cylinder heat transfer, and combustion. Finally, Fig. 16b shows that the proposed model also reproduces the NO_x emission trend quite well, capturing the decrease in NO_x levels driven by lower in-cylinder temperature peaks resulting from leaner mixtures. The NO_x emissions appear predicted with acceptable errors, the average deviation between experimental data and model results being about 82 ppm. The largest error, observed for OP #21, could be related to the combustion speed underprediction until MFB_{50} (see Fig. 15a), which led to lower in-cylinder peak temperatures that curbed the effectiveness of the Zeldovich mechanism.

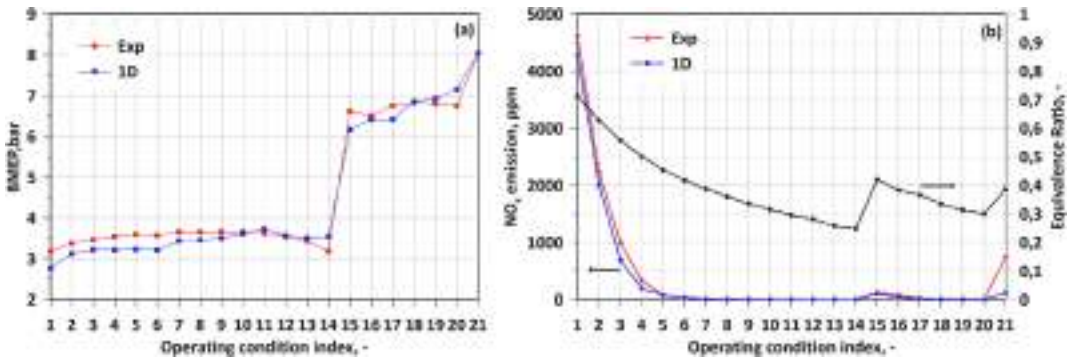

Fig. 16. Comparison between experimental data (Exp) and model predictions (1D) of engine BMEP (a) and NO_x emissions (b) for all 21 OPs.

7. Conclusions

Predicting the performance of (ultra)-lean hydrogen SI engines is a major challenge due to the interaction between flame instabilities of primarily thermo-diffusive nature and turbulence, which affects even the flame kernel formation. In this work, this prediction has been conducted with an 0D/1D engine simulation model that combines a novel 1D model for the early FK growth with a classical two-zone model for the combustion stage, accounting for both in-cylinder turbulence and TD instability. The 0D/1D model has been validated using experimental data from a single-cylinder SI engine operated at 1500 rpm in 21 operating points with equivalence ratios ranging from 0.25 to 0.71 and loads between 3 and 8 bar BMEP. The key outcomes are as follows:

- at ICE-like conditions and regardless of fuel type, the kernel formation is dominant until a radius of about 2 mm, the time to achieve which is labeled 'kernel duration';
- with lean hydrogen, the kernel duration is affected by the turbulence-enhanced TD instability, which is accounted for by replacing the LFS, S_L, with an effective flame speed, S_S;
- for all 21 OPs, the kernel durations predicted by the TD-unstable FK model match quite well (average error about 1.5 CAD) the combustion delays between ST and SoC extracted from the experimental pressure traces;
- using the predicted durations in the 0D/1D engine model leads to significant improvements in the predictions of in-cylinder pressures and burn rates, especially for ultra-lean cases;
- for almost all OPs, the main combustion angles (MFB_{10}, MFB_{50} and MFB_{75}), the BMEP values, and the NO_x emissions are estimated satisfactorily;
- modest prediction errors remain for ultra-lean OPs in the thickened flames regime, with CAD overestimations until MFB_{50} at lower loads and underestimations after MFB_{50} at higher loads.

Future developments will move in two main directions. Firstly, model refinements will be assessed to solve some residual inaccuracies, which should also enable coverage of a wider range of operating conditions and, possibly, prediction of the cycle-to-cycle variation with acceptable reliability. Secondly, the use of this 0D/1D model as a 'virtual engine' for calibration and design purposes can be envisioned and will be considered. Real-time application in engine control units, currently unfeasible due to the computational time of up to 5 min, could be achieved by post-processing the FK model results to generate, for instance, quickly accessible look-up tables.

CRediT authorship contribution statement

F. Bozza: Conceptualization, Funding acquisition, Methodology, Project administration, Software, Supervision, Writing – review & editing, Validation. **V. De Bellis:** Conceptualization, Formal analysis, Methodology, Writing – original draft, Writing – review & editing. **L. Teodosio:** Formal analysis, Methodology, Software, Validation, Visualization, Writing – original draft, Writing – review & editing. **M. Pretto:** Formal analysis, Methodology, Software, Writing – review & editing. **P. Giannattasio:** Methodology, Software, Supervision, Writing – review & editing. **R. Novella:** Data curation, Funding acquisition, Investigation, Resources, Writing – review & editing. **J. Gomez-Soriano:** Data curation, Investigation, Resources, Writing – review & editing.

Declaration of competing interest

The authors declare that they have no known competing financial interests or personal relationships that could have appeared to influence the work reported in this paper.

Data availability

Data will be made available on request.

References

[1] European Environment Agency, Climate change mitigation: reducing emissions [Online]. Available, https://www.eea.europa.eu/en/topics/in-depth/climate-change-mitigation-reducing-emissions, 2026. Accessed 10 January 2026.
[2] European Environment Agency, Greenhouse gas emissions from transport in Europe [Online]. Available, https://www.eea.europa.eu/en/analysis/indicators/greenhouse-gas-emissions-from-transport, 2025. Accessed 10 November 2025.
[3] X. Yu, S. LeBlanc, N. Sandhu, et al., Decarbonization potential of future sustainable propulsion - a review of road transportation, Energy Sci. Eng. 12 (2) (2024) 438–455, https://doi.org/10.1002/ese3.1434.
[4] K. Shahzad, I.I. Cheema, Low-carbon technologies in automotive industry and decarbonizing transport, J. Power Sources 591 (2024) 233888, https://doi.org/10.1016/j.jpowsour.2023.233888.
[5] V.J. Reddy, N.P. Hariram, R. Maity, et al., Sustainable e-fuels: green hydrogen, methanol and ammonia for carbon-neutral transportation, World Electr. Veh. J. 14 (12) (2023) 349, https://doi.org/10.3390/wevj14120349.
[6] J. Hwang, K. Maharjan, H. Cho, A review of hydrogen utilization in power generation and transportation sectors: achievements and future challenges, Int. J. Hydrog. Energy 48 (74) (2023) 28629–28648, https://doi.org/10.1016/j.ijhydene.2023.04.024.
[7] H. Goyal, P. Jones, A. Bajwa, et al., Design trends and challenges in hydrogen direct injection (H2DI) internal combustion engines, Int. J. Hydrog. Energy 86 (2024) 1179–1194, https://doi.org/10.1016/j.ijhydene.2024.08.284.
[8] S. Verhelst, Recent progress in the use of hydrogen as a fuel for internal combustion engines, Int. J. Hydrog. Energy 39 (2) (2014) 1071–1085, https://doi.org/10.1016/j.ijhydene.2013.10.102.
[9] L. Mulky, S. Srivastava, T. Lakshmi, et al., An overview of hydrogen storage technologies–key challenges and opportunities, Mater. Chem. Phys. 325 (2024) 129710, https://doi.org/10.1016/j.matchemphys.2024.129710.
[10] M.H. Esfahani, S. Zinatloo-Ajabshir, H. Naji, et al., Structural characterization, phase analysis and electrochemical hydrogen storage studies on new pyrochlore SmRETi2O7 (RE= Dy, Ho, and Yb) microstructures, Ceram. Int. 49 (1) (2023) 253–263, https://doi.org/10.1016/j.ceramint.2022.08.338.
[11] S. Zinatloo-Ajabshir, M.S. Morassaei, O. Amiri, et al., Nd2Sn2O7 nanostructures: green synthesis and characterization using date palm extract, a potential electrochemical hydrogen storage material, Ceram. Int. 46 (11) (2020) 17186–17196, https://doi.org/10.1016/j.ceramint.2020.03.014.

[12] H. Fayaz, R. Saidur, N. Razali, et al., An overview of hydrogen as a vehicle fuel, Renew. Sust. Energ. Rev. 16 (8) (2012) 5511–5528, https://doi.org/10.1016/j.rser.2012.06.012.
[13] S. Oh, C. Kim, Y. Lee, et al., Analysis of the exhaust hydrogen characteristics of high-compression ratio, ultra-lean, hydrogen spark-ignition engine using advanced regression algorithms, Appl. Therm. Eng. 215 (2022) 119036, https://doi.org/10.1016/j.applthermaleng.2022.119036.
[14] A. Onorati, R. Payri, B.M. Vaglieco, et al., The role of hydrogen for future internal combustion engines, Int. J. Engine Res. 23 (4) (2022) 529–540, https://doi.org/10.1177/14680874221081947.
[15] M. Matalon, The Darrieus–Landau instability of premixed flames, Fluid Dyn. Res. 50 (5) (2018) 051412, https://doi.org/10.1088/1873-7005/aab510.
[16] L. Berger, A. Attili, H. Pitsch, Synergistic interactions of thermodiffusive instabilities and turbulence in lean hydrogen flames, Combust. Flame 244 (2022) 112254, https://doi.org/10.1016/j.combustflame.2022.112254.
[17] W. Kim, T. Imamura, T. Mogi, R. Dobashi, Experimental investigation on the onset of cellular instabilities and acceleration of expanding spherical flames, Int. J. Hydrog. Energy 42 (21) (2017) 14821–14828, https://doi.org/10.1016/j.ijhydene.2017.04.068.
[18] X. Wen, T. Zirwes, A. Scholtissek, et al., Flame structure analysis and composition space modeling of thermodiffusively unstable premixed hydrogen flames - part II: elevated pressure, Combust. Flame 238 (2022) 111808, https://doi.org/10.1016/j.combustflame.2021.111808.
[19] B. Giménez, A. Melgar, A. Horrillo, P. Gabana, Prediction of the flame kernel growth rate in spark ignition engine fueled with natural gas, hydrogen and mixtures, Fuel 339 (2023) 126908, https://doi.org/10.1016/j.fuel.2022.126908.
[20] S. Keum, G. Zhu, R. Grover Jr., et al., A semi-empirical laminar-to-turbulent flame transition model coupled with G equation for early flame kernel development and combustion in spark-ignition engines, Int. J. Engine Res. 22 (2) (2021) 479–490, https://doi.org/10.1177/1468087419864748.
[21] R. Herweg, R.R. Maly, A fundamental model for flame kernel formation in S. I. engines, SAE Trans. 101 (1992) 1947–1976, https://www.jstor.org/stable/44611342.
[22] L. Fan, R.D. Reitz, "Development of an ignition and combustion model for spark-ignition engines," *SAE Technical Paper*, 2000–01–2809, 2000, https://doi.org/10.4271/2000-01-2809.
[23] S. Wang, Y. Li, M. Li, H. Wang, Realizing the diffusion combustion through the pre-chamber: towards heavy-duty hydrogen engines, Appl. Therm. Eng. 280 (2025) 128225, https://doi.org/10.1016/j.applthermaleng.2025.128225.
[24] S. Sfriso, F. Berni, S. Breda, et al., "Proposal and validation of 3D-CFD framework for ultra-lean hydrogen combustion in ICEs," *SAE Technical Paper*, 2024–01–2685, 2024, https://doi.org/10.4271/2024-01-2685.
[25] H.E. Gülcan, H. Gürbüz, Effect of spark plug position and ignition timing on performance, exergy, exergoeconomic, environmental, and enviro-cost in a hydrogen-SI engine, Appl. Therm. Eng. 278 (2025) 127400, https://doi.org/10.1016/j.applthermaleng.2025.127400.
[26] J.J. Thomas, I. Bortel, Š. Kyjovský, et al., Mitigation of abnormal combustion in hydrogen-fuelled SI engines via ignition system optimisation and water injection, Int. J. Hydrog. Energy 200 (2026) 152822, https://doi.org/10.1016/j.ijhydene.2025.152822.
[27] M. Pretto, P. Giannattasio, E. De Betta, F. Bozza, A consistent model of the initiation, early expansion, and possible extinction of a spark-ignited flame kernel, Int. J. Engine Res. 26 (2) (2024) 161–175, https://doi.org/10.1177/14680874241272812.
[28] D. Yu, Z. Chen, Theoretical analysis on the transient ignition of a premixed expanding flame in a quiescent mixture, J. Fluid Mech. 924 (2021) A22, https://doi.org/10.1017/jfm.2021.633.
[29] M. Pretto, F. Bozza, P. Giannattasio, et al., "Validation of an Integrated Ignition-Combustion Model for Premixed Hydrogen-Air Flames under Lean Conditions," *SAE Technical Paper*, 2025-32-0056, 2025, https://doi.org/10.4271/2025-32-0056.
[30] T.L. Howarth, E.F. Hunt, A.J. Aspden, Thermodiffusively-unstable lean premixed hydrogen flames: phenomenology, empirical modelling, and thermal leading points, Combust. Flame 253 (2023) 112811, https://doi.org/10.1016/j.combustflame.2023.112811.
[31] A. Onorati, G. Montenegro, State of the art of 1D thermo-fluid dynamic simulation models, in: 1D and multi-D Modeling techniques for IC engine simulation, SAE International, Warrendale, PA, USA, 2020, pp. 1–26, https://doi.org/10.4271/9780768099522.
[32] M. Pretto, E. De Betta, P. Giannattasio, Estimating the minimum ignition energy of spark-ignited fuel/air mixtures: preliminary steps towards a novel modelling approach, J. Phys. Conf. Ser. 2893 (1) (2024) 012093, https://doi.org/10.1088/1742-6596/2893/1/012093.
[33] G. Meyer, A. Wimmer, A thermodynamic model for the plasma kernel volume and temperature resulting from spark discharge at high pressures, J. Therm. Anal. Calorim. 133 (2) (2018) 1195–1205, https://doi.org/10.1007/s10973-018-7169-z.
[34] M. Pretto, P. Giannattasio, V. Grahn, et al., Experimental investigation of the early development of spark-ignited CH4-air and C3H8-air flame kernels, Fuel 394 (2025) 135110, https://doi.org/10.1016/j.fuel.2025.135110.
[35] Y. Ko, V.S. Arpaci, R.W. Anderson, Spark ignition of propane-air mixtures near the minimum ignition energy: part II. A model development, Combust. Flame 83 (1–2) (1991) 88–105, https://doi.org/10.1016/0010-2180(91)90205-P.
[36] D.G. Goodwin, H.K. Moffat, I. Schoegl, et al., Cantera: An object-oriented software toolkit for chemical kinetics, thermodynamics, and transport processes - Version 3.1.0 [Online]. Available, https://zenodo.org/records/14455267, 2024.
[37] G. Smith, D.M. Golden, M. Frenklach, et al., GRI-Mech 3.0 [Online]. Available, http://www.me.berkeley.edu/gri_mech/.
[38] UC San Diego Combustion Research Group, The San Diego Mechanism - Chemical-Kinetic Mechanisms for Combustion Applications [Online]. Available, http://web.eng.ucsd.edu/mae/groups/combustion/mechanism.html, 2025. Accessed 3 June.
[39] Y. Zhang, J. Fu, M. Xie, J. Liu, Improvement of H_2/O_2 chemical kinetic mechanism for high pressure combustion, Int. J. Hydrog. Energy 46 (7) (2021) 5799–5811, https://doi.org/10.1016/j.ijhydene.2020.11.083.
[40] Z. Zhou, F.E. Hernández-Pérez, Y. Shoshin, et al., Effect of Soret diffusion on lean hydrogen/air flames at normal and elevated pressure and temperature, Combustion Theory Model. 21 (5) (2017) 879–896, https://doi.org/10.1080/13647830.2017.1311028.
[41] J.K. Bechtold, M. Matalon, The dependence of the Markstein length on stoichiometry, Combust. Flame 127 (1–2) (2001) 1906–1913, https://doi.org/10.1016/S0010-2180(01)00297-8.
[42] A. Moroshkina, A. Ponomareva, V. Mislavskii, et al., Activation energy of hydrogen-methane mixtures, Fire 7 (2) (2024) 42, https://doi.org/10.3390/fire7020042.
[43] G. Jomaas, C.K. Law, J.K. Bechtold, On transition to cellularity in expanding spherical flames, J. Fluid Mech. 583 (2007) 1–26, https://doi.org/10.1017/S0022112007005885.
[44] C.K. Law, C.J. Sung, Structure, aerodynamics, and geometry of premixed flamelets, Prog. Energy Combust. Sci. 26 (4–6) (2000) 459–505, https://doi.org/10.1016/S0360-1285(00)00018-6.
[45] C. Altantzis, C.E. Frouzakis, A.G. Tomboulides, et al., Hydrodynamic and thermodiffusive instability effects on the evolution of laminar planar lean premixed hydrogen flames, J. Fluid Mech. 700 (2012) 329–361, https://doi.org/10.1017/jfm.2012.136.
[46] S. Molina, S. Ruiz, J. Gómez-Soriano, M. Olcina-Girona, Impact of hydrogen substitution for stable lean operation on spark ignition engines fueled by compressed natural gas, Results Eng. 17 (2023) 100799, https://doi.org/10.1016/j.rineng.2022.100799.
[47] M. Pochet, H. Jeanmart, F. Contino, Uncertainty quantification from raw measurements to post-processed data: a general methodology and its application to a homogeneous-charge compression–ignition engine, Int. J. Engine Res. 21 (9) (2020) 1709–1737, https://doi.org/10.1177/1468087419892697.
[48] Convergent Science, Inc, CONVERGE CFD software [Online]. Available, https://convergecfd.com, 2025. Accessed 8 July.
[49] R. Novella, J. Gomez-Soriano, D. González-Domínguez, O. Olaciregui, Understanding the role of thermo-diffusive instabilities in hydrogen combustion for lean-burn spark-ignition engine operation, Energy Convers. Manag. 334 (2025) 119801, https://doi.org/10.1016/j.enconman.2025.119801.
[50] F. Bozza, A. Gimelli, S.S. Merola, B.M. Vaglieco, Validation of a fractal combustion model through flame imaging, SAE Trans. 114 (2005) 973–987, http://www.jstor.org/stable/44722057.
[51] F. Bozza, L. Teodosio, V. De Bellis, et al., A refined 0D turbulence model to predict tumble and turbulence in SI engines, SAE Int. J. Engines 12 (1) (2019) 15–30, https://doi.org/10.4271/03-12-01-0002.
[52] S. Lapointe, G. Blanquart, Fuel and chemistry effects in high Karlovitz premixed turbulent flames, Combust. Flame 167 (2016) 294–307, https://doi.org/10.1016/j.combustflame.2016.01.035.
[53] V. De Bellis, F. Bozza, D. Tufano, A comparison between two phenomenological combustion models applied to different SI engines, in: SAE Technical Paper, 2017, https://doi.org/10.4271/2017-01-2184, 2017–01–2184.
[54] G.A. Lavoie, J.B. Heywood, J.C. Keck, Experimental and theoretical study of nitric oxide formation in internal combustion engines, Combust. Sci. Technol. 1 (4) (1970) 313–326, https://doi.org/10.1080/00102206908952211.